

# Synthesis of Magnetic Targeted Cellulose Composite Decorated with Poly(AA-DMC) for Synergistic Adsorption Degradation of Congo Red from Organic Wastewater

**Chen Ling**

Changsha University of Science and Technology

**Dai Yimin** (✉ [yimindai@sohu.com](mailto:yimindai@sohu.com))

Changsha University of Science and Technology

**Lu Qi**

Changsha University of Science and Technology

**Fang Chengqian**

Changsha University of Science and Technology

**Wang Zhiheng**

Changsha University of Science and Technology

**Wang Shengyun**

Changsha University of Science and Technology

**Zhang Yue-fei**

Changsha University of Science and Technology

**Li Yan**

Changsha University of Science and Technology

**Wan Li**

Changsha University of Science and Technology

---

## Research Article

**Keywords:** Cellulose, MnFe<sub>2</sub>O<sub>4</sub>, Poly(AA-DMC), Peroxymonosulfate, Magnetic separation, Congo red

**Posted Date:** May 11th, 2021

**DOI:** <https://doi.org/10.21203/rs.3.rs-453687/v1>

**License:**   This work is licensed under a Creative Commons Attribution 4.0 International License.

[Read Full License](#)

---

1 **Synthesis of Magnetic Targeted Cellulose Composite Decorated with**  
2 **Poly(AA-DMC) for Synergistic Adsorption Degradation of Congo**  
3 **Red from Organic Wastewater**

4 Chen Ling, Dai Yimin\*, Lu Qi, Fang Chengqian, Wang Zhiheng, Wang Shengyun,

5 Zhang Yue-fei, Li Yan, Wan Li\*

6 *School of Chemistry and Food Engineering, Hunan Provincial Key Laboratory of Materials Protection for*  
7 *Electric Power and Transportation, Changsha University of Science and Technology, Changsha 410114, PR China*

8

9 **Abstract:** A brand-new environmental-friendly magnetic cellulosic adsorbent  
10  $\text{MnFe}_2\text{O}_4@\text{Cel-g-p(AA-DMC)}$  was synthesized by natural cellulose and  
11 easy-recovered magnetic particles  $\text{MnFe}_2\text{O}_4$ . Magnetic cellulose composites were  
12 characterized by SEM, TEM, XPS, XRD, BET, VSM, TGA and FTIR. The  
13  $\text{MnFe}_2\text{O}_4\text{NPs}$  could activate the peroxymonosulfate (PMS) to produce various  
14 reactive oxygen species (ROS). Accordingly, magnetic cellulose composites can  
15 synergistic adsorption degradation of dyes from organic wastewater. The Congo red  
16 (CR) removal efficiency by  $\text{MnFe}_2\text{O}_4@\text{Cel-g-p(AA-DMC)}$  via PMS activated by  
17  $\text{MnFe}_2\text{O}_4$  reached a maximum of 96.9% and only 9% reduction after four  
18 adsorption-desorption cycles, indicating the stability and recoverability of adsorbent.  
19 It is worth noting that adsorbents can be quickly recovered from aqueous solution by  
20 external magnet owing to superior saturation magnetization ( $35.44 \text{ emu}\cdot\text{g}^{-1}$ ). A  
21 possible degradation mechanism of CR on the  $\text{MnFe}_2\text{O}_4@\text{Cel-g-p(AA-DMC)}$

22 \* Corresponding authors. Tel.: +86 0731 85258733; fax: +86 0731 85258733;

23 E-mail address: yimindai@sohu.com (Dai Y. M.), wanli@ms.giec.ac.cn (Wan L.)

1 composite was proposed. The results suggest that adsorbent display strong potential  
2 for the removal of CR dyes from organic wastewater.

3 **Keywords:** Cellulose,  $\text{MnFe}_2\text{O}_4$ , Poly(AA-DMC), Peroxymonosulfate, Magnetic  
4 separation, Congo red

5

## 6 **1. Introduction**

7 Facing the current severe ecological environmental problems, the global  
8 endeavor committed themselves to improve present situation (Sanna et al. 2016).  
9 Especially, the rapid development of textile, paper industry, cosmetics and other  
10 industries caused an unnegligible water pollution, which gradually put the  
11 environment and human health in danger (Anjum et al. 2019; Malatji et al. 2020). The  
12 worldwide dye consumption of the industries was close to 800,000 tons/year  
13 according to incomplete statistics (Chaudhary et al. 2013). Therefore, to cope with the  
14 rapid diffusion of dye wastewater, we urgently need a more effective treatment.  
15 Membrane separation, flocculation, advanced oxidation and adsorption seem available  
16 techniques frequently used in general (Kamel et al. 2020; An et al. 2019). If  
17 adsorption techniques did indeed apply to adsorb pollutants simply and effectively, we  
18 would certainly lean to use this easy-designed and low-consumption process (Anjum  
19 et al. 2019; Moharrami et al. 2020; Zhang et al. 2020). From the point of view, finding  
20 green and environmental-friendly adsorbents had been a brand-new test owing to its  
21 numerous unique properties.

22 When it comes to green materials, we firstly thought inorganic bio-adsorbents  
23 like Cellulose (Cel), the most abundant natural polysaccharide, which was isolated  
24 from lignocellulosic sources such as wood, cotton, forest residues, agricultural or

1 fruits wastes, bacterial cellulose and so on (Liu et al. 2014; Shi et al. 2021).  
2 Cellulose-based material was always taken for an effective compound for eliminating  
3 contaminant in the water (Jiang et al. 2020; Wang et al. 2019), because it represent  
4 notable opportunities due to its low-cost, biocompatibility, renewability,  
5 environmental biodegrade ability, facile chemical modification, excellent mechanical  
6 capacities and large surface area (Jiang et al. 2020; Wang et al. 2019; An et al. 2017;  
7 Amiralian et al. 2020). A great deal of hydrophilic, as well as highly reactive hydroxyl  
8 and carboxyl groups existed in their polymeric scaffold, which played an active part  
9 in surface modifications, other substance could fairly easy grafting on the second,  
10 third and sixth carbon atoms (Arabkhani et al. 2020; Li et al. 2020). Cellulosic  
11 materials provided a great deal of attachment plaques and adsorption sites for organic  
12 contaminants as a result of their high specific surface area and porous structure  
13 (Kamel et al. 2020; Chen et al. 2020). In the meantime, the surface modification of  
14 cellulose was beneficial to improve its application fields (Alekseeva et al. 2017)

15 According to the literature, grafting hydrophilic monomers in the presence of  
16 cross linker could improve the utilization efficiency of wastewater with organic dyes.  
17 Acrylic acid monomer (AA) was introduced to react with Cel to connect  
18 polymerizable double bonds, and 2-methacryloyloxyethyl trimethylammonium  
19 chloride (DMC) was adopted to charge the Cel grafting co-polymer (Tian et al. 2012).  
20 Both AA and DMC were hydrophilic monomers and contain a large number of double  
21 bonds but cellulose modified by two monomers had not been widely used in  
22 wastewater containing dyes (Wang et al. 2019).

23 Common separation ways such as centrifugation and filtration were hard to  
24 isolate adsorbent. Combination of cellulose with magnetic nanoparticles was a

1 feasible method, since magnetic cellulose composites as effective carriers (Lu et al.  
2 2019), possessed great adsorption performance not only in averting the aggregation of  
3 nanoparticles, but also in facile magnetic separation (Kalantari et al. 2020). The  
4 general formula of spinel-type ferrite nanoparticles (NPs) was usually represented as  
5  $MFe_2O_4$ ,  $M=Mn, Co, Ni, Cu$  (Pang et al. 2016; Qian et al. 2020). Among these NPs,  
6  $MnFe_2O_4$ , contrast to other spinel ferrites ( $NiFe_2O_4, CoFe_2O_4, ZnFe_2O_4$ , etc.) used as  
7 heterogeneous catalyst, had superior physical and chemical properties, high content in  
8 soil, and hypotoxicity to the environment (Wang et al. 2020; Mady et al. 2019).  
9 However, the mentioned compounds containing transition metals had a catalytic effect  
10 on peroxymonosulfate (PMS) to generate various reactive oxygen species (ROS),  
11 such as sulfate radical ( $SO_4^{\cdot-}$ ), hydroxyl radical ( $\cdot OH$ ), superoxide radical anion ( $O_2^{\cdot-}$ )  
12 and singlet oxygen ( $^1O_2$ ) (Zhou et al. 2020; Lops et al. 2019). In contrast to  $H_2O_2$ ,  
13 PMS was an ideal oxidant due to its low cost, water-soluble and high chemical  
14 stability (Wang et al. 2014). It was worth noting that metal nanoparticles with  
15 nanometer-scale dimensions were unstable and aggregating because of the high  
16 surface area and surface energy. To avoid aggregation of metal NPs, it was an  
17 effective way to immobile metal NPs onto substrates (Lu et al. 2019). This thesis  
18 intended to use cellulose as substrates to support metal-oxides for preparing  
19  $MnFe_2O_4$ /cellulose hybrids (Yao et al. 2014). By the way,  $MnFe_2O_4$ NPs not only  
20 activate PMS to generate ROS for oxidation of organic pollutions, but it could be  
21 easily collected by external magnetic field (Zhao et al. 2017). Special mention also  
22 should be made of  $MnFe_2O_4$  itself as a kind of excellent photocatalytic material for  
23 wastewater treatment (Desai et al. 2020).

24 The aim of this case was to obtain magnetic cellulose composites and apply to

1 remove organic dyes. All samples including optimum pH, reaction time, adsorption  
2 kinetics and adsorption isotherm were characterized using series of analytical tools,  
3 such as XRD, XPS, SEM, TEM, BET, TGA. This paper provided a simple method to  
4 prepare a new cellulose-based material and introduced its application for the removal  
5 of Congo red dye.

## 6 **2. Experimental**

### 7 2.1 Materials

8 Cellulose (powder, 250  $\mu\text{m}$ ), acrylic acid (AA), 2-methacryloyloxyethyl  
9 trimethylammonium chloride (DMC), N, N'-Methylenebis (acrylamide) (MBA),  
10 potassium persulfate (KPS), glutaraldehyde, manganese(II) nitrate tetrahydrate  
11 ( $\text{Mn}(\text{NO}_3)_2 \cdot 4\text{H}_2\text{O}$ ), ferric nitrate nonahydrate ( $\text{Fe}(\text{NO}_3)_3 \cdot 9\text{H}_2\text{O}$ ), ethanol, hydrochloric  
12 acid (HCl), sodium hydroxide (NaOH), Congo red (CR) were purchased from aladdin.  
13 All chemicals were analytical grade and used without further purification.

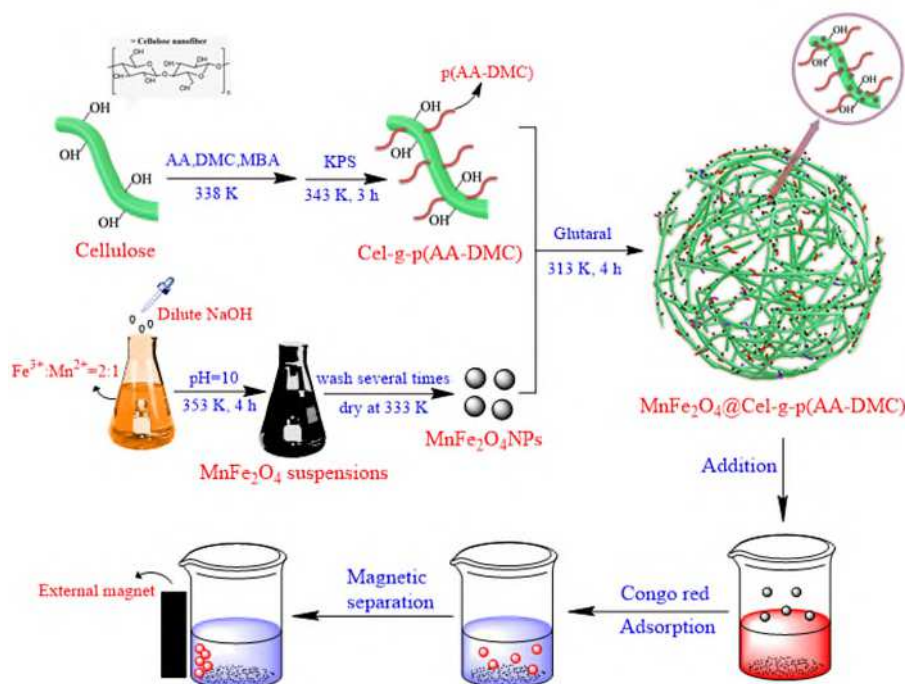
### 14 2.2 Synthesis of $\text{MnFe}_2\text{O}_4$ NPs

15 The synthesis of  $\text{MnFe}_2\text{O}_4$  was carried out by co-precipitation method based on  
16 previous research with a little change (Yao et al. 2014). Appropriate amount of  
17  $\text{Fe}(\text{NO}_3)_3 \cdot 9\text{H}_2\text{O}$  and  $\text{Mn}(\text{NO}_3)_2 \cdot 4\text{H}_2\text{O}$  were mixed and completely dissolved in  
18 distilled water (1 mol  $\text{Fe}^{3+}$  : 12.5 L distilled water). The molar ratio of  $\text{Fe}^{3+}$  and  $\text{Mn}^{2+}$   
19 was theoretically 2:1. During constant magnetic stirring, the appropriate amount of  
20 dilute sodium hydroxide solution ( $0.5 \text{ mol} \cdot \text{L}^{-1}$ ) were breathed into the above  
21 dispersion until the pH of the mixture reached 10, then stirred at  $80^\circ\text{C}$  for 4 h. Filter  
22 out the prepared precipitate, rinse with deionized water, and dry at  $60^\circ\text{C}$  reaching a  
23 constant mass (Pineda et al. 2021). Finally, all samples were stored in desiccator.

### 24 2.3 Preparation of Cel-g-p(AA-DMC) composites

1           7 g NaOH and 12 g urea were mixed with 81 ml distilled water, of which the  
 2 proportions equal to 7:12:81. The above mixture was stirred until no lumpy particles  
 3 in the solution. Then 2.0 g cellulose powder was added into the NaOH/urea/H<sub>2</sub>O  
 4 solution pre-cooled at -12 °C for 2 h. The mixture solution was stirred for 5 min and  
 5 then preserved at -12 °C for about 2 h until solution was transparent (Luo et al. 2013;  
 6 Zhou et al. 2005). 4 ml AA, 8 ml DMC and 0.15 g MBA were added to 20 ml above  
 7 obtained solution, and heat the mixture to 65 °C. Then 0.1 g KPS was dissolved in 10  
 8 ml distilled water and poured into above solution to initiate the reaction with stirring  
 9 at 70 °C for 3 h (Malatji et al. 2020). The resulting gel was rinsed repeatedly with  
 10 ethanol and distilled water, then dried in a vacuum oven at 70 °C reaching a constant  
 11 weight.

12 2.4 Preparation of MnFe<sub>2</sub>O<sub>4</sub>@Cel-g-p(AA-DMC) composites



13  
 14 **Fig 1.** Schematic diagram of synthesis and adsorption of the  
 15 MnFe<sub>2</sub>O<sub>4</sub>@Cel-g-p(AA-DMC) nanohybrid.

16 Fig. 1 showed schematic diagram of synthesis and adsorption of the

1 MnFe<sub>2</sub>O<sub>4</sub>@Cel-g-p(AA-DMC) nanohybrid. 1.0 g cellulose grafted with AA and DMC  
2 was dissolved in conical flask of 60 ml distilled water and injected 1 ml  
3 glutaraldehyde dropwise. Glutaraldehyde, as a cross-linker, was used to trigger a  
4 cross-link reaction in the presence of cellulose and MnFe<sub>2</sub>O<sub>4</sub>NPs (Chen et al. 2019).  
5 Subsequently, 1.0 g MnFe<sub>2</sub>O<sub>4</sub> NPs was added to above solution and ultrasonic  
6 dispersion uniformity. The mixture was continuously stirred at 40 °C for 4 h. The  
7 obtained composites were rinsed in distilled water in order to remove unreacted  
8 cellulose, then dried in the vacuum oven at 60 °C for 12 h.

## 9 2.4 Characterization

10 The scanning electron microscopy (SEM) and transmission electron microscopy  
11 (TEM) were used to analyze the morphology of the MnFe<sub>2</sub>O<sub>4</sub> and  
12 MnFe<sub>2</sub>O<sub>4</sub>@Cel-g-p(AA-DMC). X-ray diffraction (XRD) analysis of MnFe<sub>2</sub>O<sub>4</sub> and  
13 MnFe<sub>2</sub>O<sub>4</sub>@Cel-g-p(AA-DMC) was conducted on a Bruker D8 Advance X-ray  
14 diffractometer (Bruker, Karlsruhe, Germany). The XPS experiments were conducted  
15 on an X-ray photoelectron spectroscopy (XPS, K-Alpha, Thermo Fisher Scientific).  
16 The surface area and pore size distribution were determined by N<sub>2</sub>  
17 adsorption-desorption isotherms with an ASAP2010 analyzer (Micromeritics).  
18 Thermogravimetric analysis (TGA) was conducted on a thermal analyser (Mettler  
19 Toledo TGA/DTA851) in the range of 40-550 °C at a heating rate of 10 °C·min<sup>-1</sup>  
20 under the flow of air. FT-IR spectra were obtained using a UK Inter-spec 2020  
21 spectrolab spectrometer in the range of 500 to 4000 cm<sup>-1</sup>. Magnetic measurements of  
22 samples were performed using a vibrating sample magnetometer (VSM). The residual  
23 concentration change of the dye solution was calculated by UV-VIS  
24 spectrophotometer (UV-2450, Shimadzu, Japan) (Kalantari et al. 2020; Chen et al.

1 2019).

## 2 2.5 Evaluation of Catalytic Performance

3 Adsorption studies of Congo red (CR) dye from aqueous phase were performed  
4 using 50 ml of CR solution with different initial dye concentrations in 100 ml conical  
5 flask. This flask was placed on a shaker with a continuous shaking speed of 200 rpm.  
6 30.0 mg of MCA was added to the solution while shaking for 3 h at room temperature  
7 to reach adsorption equilibrium. Then the samples were centrifuged at 3400 rpm for  
8 10 min and took the supernatant for analysis by a UV-Vis spectrophotometer with its  
9 absorption at maximum absorption wavelength (497 nm) of CR. Calculated the  
10 equilibrium adsorption capacity ( $q_e$ ) ( $\text{mg}\cdot\text{g}^{-1}$ ) and adsorption rate (R%) according to  
11 the following formula:

$$12 \quad R\% = \frac{(C_0 - C_e)}{C_0} \times 100\% \quad (1)$$

$$13 \quad q_e = (C_0 - C_e) \times \frac{V}{M} \quad (2)$$

14 Where (Huang et al. 2020),  $C_0$  and  $C_e$  ( $\text{mg}\cdot\text{L}^{-1}$ ) were the initial and the equilibrium  
15 concentrations of CR, respectively.  $q_0$  was the equilibrium adsorption capacity of  
16 prepared adsorbent.  $M$  (g) was the mass of the adsorbent put into the system and  $V$   
17 (mL) was the total volume of the system.

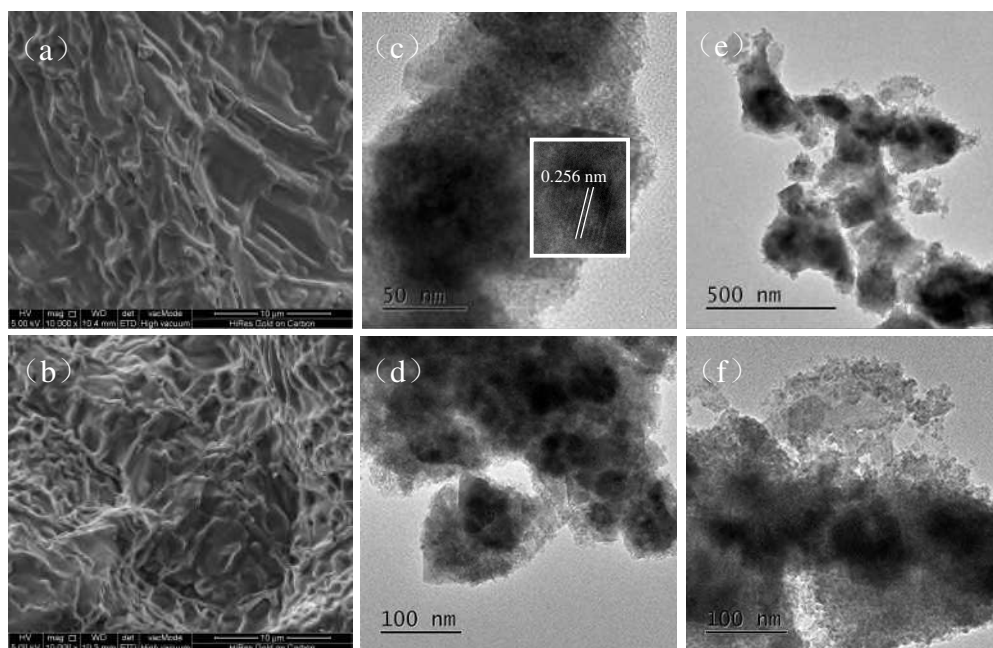
## 18 3. Results and Discussion

### 19 3.1 Characterization of prepared adsorbents

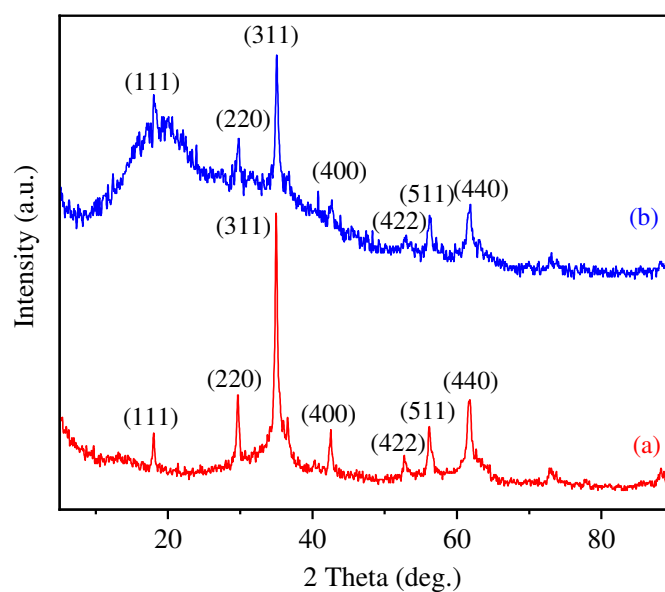
20  $\text{MnFe}_2\text{O}_4@\text{Cel-g-p}(\text{AA-DMC})$ , SEM and TEM were performed to examine the  
21 morphology and structure of the  $\text{MnFe}_2\text{O}_4$ . As could be seen from Fig. 2 (a) and (b),  
22 cellulose grafted by AA and DMC presented an unsmooth reticular formulation with a  
23 rough surface and stuffed pore, which immensely increased the surface area of  
24 copolymer (Wang et al. 2019; Chen et al. 2019). In Fig. 2 (c) and (d), the bare

1 MnFe<sub>2</sub>O<sub>4</sub> crystals showed an irregular shape morphology with severe aggregation.  
2 The inset of TEM images of single MnFe<sub>2</sub>O<sub>4</sub> NPs clearly showed the lattice fringes  
3 with an interplanar spacing of 0.256 nm, which corresponds to the (311) plane of  
4 spinel MnFe<sub>2</sub>O<sub>4</sub> (Wang et al. 2020; Zhou et al. 2020). Fig. 2 (e) and (f) showed the  
5 images of MnFe<sub>2</sub>O<sub>4</sub>@Cel-g-p(AA-DMC) magnetic nanoparticles which were  
6 concentrated in the black core region and the modified cellulose were loaded in the  
7 outer transparent region. The results could speculate the successful synthesis of  
8 MnFe<sub>2</sub>O<sub>4</sub>@Cel-g-p(AA-DMC) and it probably took on core-shell structure.

9 The crystallinity and phase purity of the MnFe<sub>2</sub>O<sub>4</sub>NPs (a) and  
10 MnFe<sub>2</sub>O<sub>4</sub>@Cel-g-p(AA-DMC) NPs (b) were analyzed by XRD, as shown in Fig. 3.  
11 The XRD patterns of MnFe<sub>2</sub>O<sub>4</sub> sample contained diffraction peaks at  $2\theta = 18.18^\circ$ ,  
12  $29.78^\circ$ ,  $35.08^\circ$ ,  $42.58^\circ$ ,  $52.78^\circ$ ,  $56.28^\circ$  and  $61.78^\circ$ , which were all indexed to the  
13 crystal planes of spinel ferrite (111), (220), (311), (400), (422), (511) and (440),  
14 respectively. All the diffraction peaks in the XRD pattern were consistent with the  
15 cubic spinel MnFe<sub>2</sub>O<sub>4</sub> (Pang et al. 2016) Compared with pure MnFe<sub>2</sub>O<sub>4</sub>, the  
16 diffraction peaks of MnFe<sub>2</sub>O<sub>4</sub>@Cel-g-p(AA-DMC) were slightly change in (111)  
17 plane, this may be due to the low content of cellulose caused by the low intensity of  
18 characteristic peaks and air scattering (Wang et al. 2020; Ghanbari et al. 2019).



1 **Fig 2.** SEM images of Cel-g-p(AA-DMC) (a, b), HR-TEM images of MnFe<sub>2</sub>O<sub>4</sub> (c, d)  
 2 and MnFe<sub>2</sub>O<sub>4</sub>@Cel-g-p(AA-DMC) (e, f).



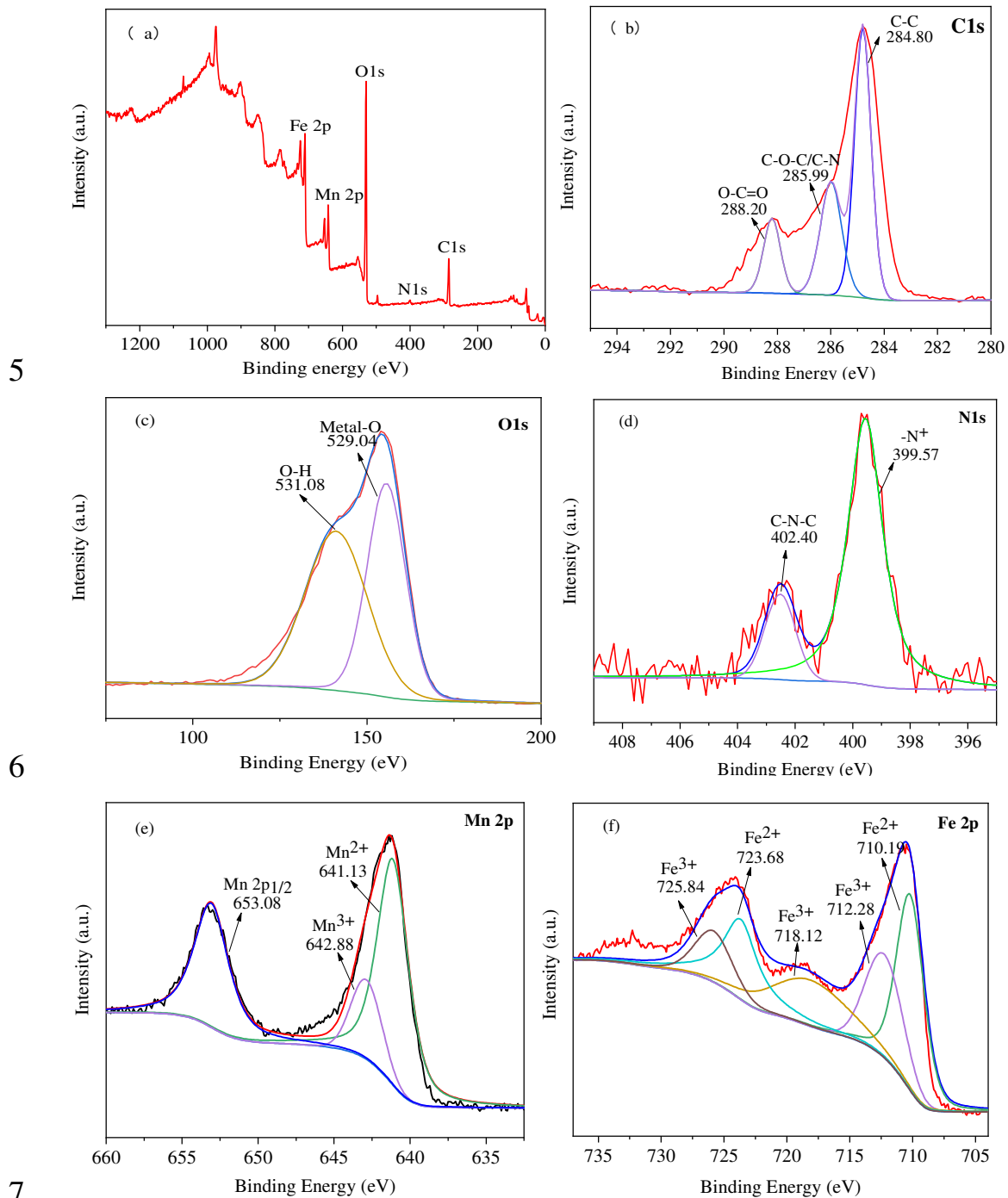
3  
 4 **Fig 3.** XRD pattern of MnFe<sub>2</sub>O<sub>4</sub> (a), MnFe<sub>2</sub>O<sub>4</sub>@Cel-g-p(AA-DMC) (b).

5 To further confirm the surface elemental composition and electronic states of the  
 6 prepared materials, the results of XPS had been shown in Fig. 4. As we can see,  
 7 elements C, O, N, Fe and Mn coexisted in composite samples. The high-resolution  
 8 spectrum of Fe2p showed obvious Fe<sup>2+</sup> (710.19 eV and 723.68 eV) and Fe<sup>3+</sup> (712.28

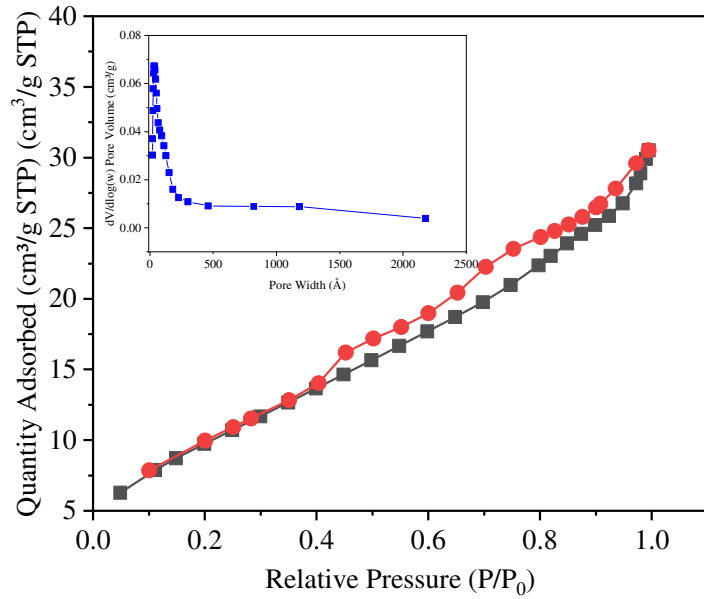
1 eV and 725.84 eV) binding energy peaks of  $2p_{3/2}$  and  $2p_{1/2}$ , respectively. A satellite  
2 peak at 718.12 eV may be attributed to the presence of  $Fe^{3+}$ . As showed in the Mn 2p  
3 spectrum, two distinct peaks at 641.13 eV and 653.08 eV, which were assigned to the  
4 binding energy of  $2p_{3/2}$  and  $2p_{1/2}$ , respectively. A satellite peak at 642.88 eV indicated  
5 the presence of  $Mn^{2+}$  (Wang et al. 2020). For the XPS spectra of O1s, two main peaks  
6 at binding energies of 529.64 eV and 531.08 eV can be observed. This may because of  
7 the presence of the lattice oxygen of metal oxides (Metal-O) and adsorbed oxygen or  
8 surface hydroxyl species (O-H) of the adsorbents (Chen et al. 2019). The typical  
9 binding energies at 399.57 eV and 402.40 eV belong to  $-(CH_2)_2-N^+(CH_3)_2$  and  
10  $NH_2CO^-$ , respectively (Wang et al. 2019). The C1s spectrum of  
11  $MnFe_2O_4@Cel-g-p(AA-DMC)$  possessed three peaks located at 284.8, 285.99 and  
12 286.3 eV, respectively. The peak at 284.8 eV was related to C-C bonds in  
13 hydrocarbons, particularly methyl and methylene groups of cellulose structure. The  
14 peak at 285.99 eV was attributed to C-O bonds in hydroxyl (C-OH) and ether (C-O-C)  
15 groups which also could speculate the presence of C-N bonds grafting DMC. The  
16 weak peak appeared at about 288.20 eV could be attributed to the formation of ester  
17 bonds due to the grafting of AA and DMC (Wang et al. 2019). Based on above results,  
18 we draw a conclusion that the combination of  $MnFe_2O_4$  and the grafting of AA and  
19 DMC (Zhou et al. 2020), which indicated the  $MnFe_2O_4@Cel-g-p(AA-DMC)$  had  
20 been successfully synthesized.

21  $N_2$  adsorption-desorption isotherms and the BJH pore size distribution of  
22  $MnFe_2O_4@Cel-g-p(AA-DMC)$  were shown in Fig. 5. On the basis of IUPAC  
23 classification, the  $N_2$  adsorption-desorption isotherms were of type IV with an  
24 obvious hysteresis loop of type H3, showing a representative mesoporous material

1 (Desai et al. 2020). The BET surface area, pore size and pore volume were 38.34  
2  $\text{m}^2\cdot\text{g}^{-1}$ , 49.19 Å and  $0.047 \text{ cm}^3\cdot\text{g}^{-1}$  for prepared composites, respectively. It was  
3 certified that the sample had porous structure been rich in mesoporous and  
4 microporous.



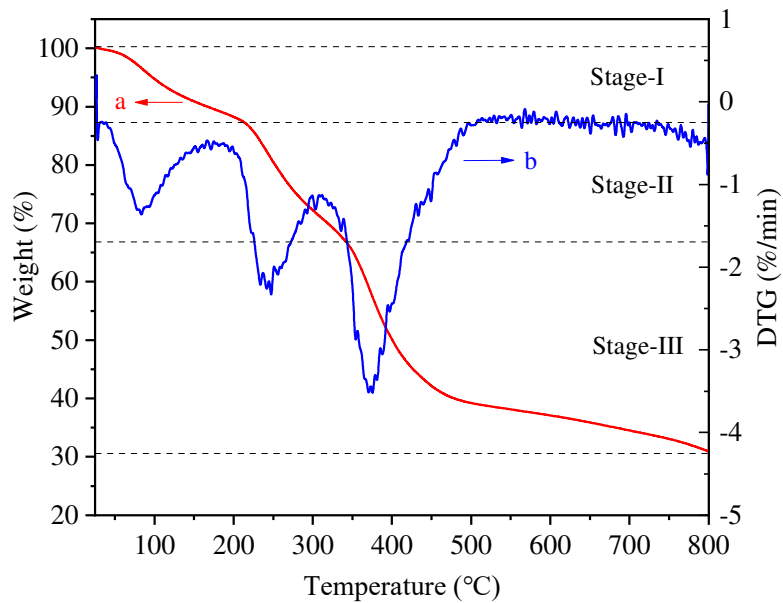
8 **Fig 4.** XPS survey (a), C1s (b), O1s (c), N1s (d), Mn 2p (e) and Fe 2p (f) spectra of  
9 MnFe<sub>2</sub>O<sub>4</sub>@Cel-g-p(AA-DMC).



1

2 **Fig 5.** Nitrogen adsorption–desorption isotherms and the BJH pore size distributions

3 of MnFe<sub>2</sub>O<sub>4</sub>@Cel-g-p(AA-DMC).



4

5 **Fig 6.** TG-DTG curve of the MnFe<sub>2</sub>O<sub>4</sub>@Cel-g-p(AA-DMC).

6 Thermo-gravimetric-derivative thermal gravimetric (TG-DTG) analyzed the ratio  
7 of loaded magnetic nanoparticles and thermostability of the complex polysaccharides.

8 As shown in Fig. 6, three-stage weight loss was observed for the

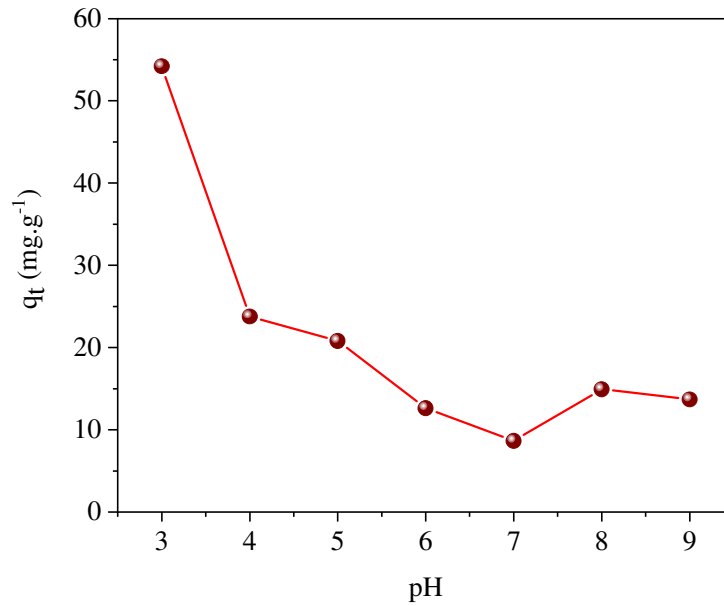
9 MnFe<sub>2</sub>O<sub>4</sub>@Cel-g-p(AA-DMC). Stage-I generated in the temperature range of ambient

1 temperature to 215°C, which mainly due to the evaporation of water in cellulose.  
2 Stage-II gave rise to major weight loss at temperatures between 215-350°C, which  
3 was associated with the thermal decomposition of nanocellulose polymer chains.  
4 Stage-III showed slow decomposition above 350°C, which was attributed to the  
5 decomposition of the nanocomplex. By reason of the foregoing, about 70% of the  
6 composite was thermal degradation, leaving about 30% residue (Sajjadi et al. 2019).  
7 Multiple stages of decomposition were observed from the TG-DTG curves, this may  
8 be accounted for incorporation of MnFe<sub>2</sub>O<sub>4</sub> magnetic NPs reducing the thermal  
9 degradation of modified nanocellulose.

## 10 3.2 Catalytic Evaluation

### 11 3.2.1 Effect of pH

12 pH of reaction system was one of the key factors of affecting the adsorption  
13 performance for dyes. The concentration of the CR and the amount of  
14 MnFe<sub>2</sub>O<sub>4</sub>@Cell-g-p(AA-DMC) remained unchanged, and the initial value of pH of  
15 the system was controlled to shift from 3 to 9 by adjusting the amounts of NaOH and  
16 HCl. As presented in Fig. 7, the adsorption capacity was significantly reduced with  
17 the pH increasing from 3 to 7. The adsorption capacity increased slightly at pH above  
18 7 under alkaline conditions which could explain the fact that CR being an anionic dye  
19 adsorbed onto the positive adsorbent surface in acidic environment. In this work, the  
20 optimal pH of the system was 3 when the adsorption capacity showed higher value  
21 (Amiralian et al. 2020; Wo et al. 2019).



1

2 **Fig 7.** The effect of pH on the adsorption capacity ( $q_t$ ) of CR (reaction conditions:

3 [dye]=0.08 g.L<sup>-1</sup>, [adsorbent]=0.05 g, T=298 K).

4 3.2.2 Impact of contact time and adsorption kinetics

5 We investigated the influence of contact time on the removal of Congo red dye

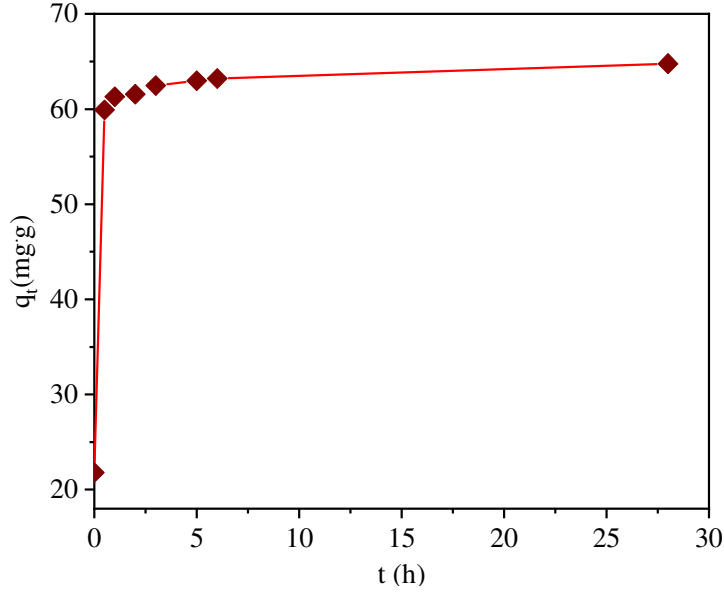
6 by applying the MnFe<sub>2</sub>O<sub>4</sub>@Cell-g-p(AA-DMC) composites as adsorbents. With time

7 passing, the adsorption capacity continued to increase until it approached equilibrium.

8 This was because the surface area of cellulose could expand after continuous water

9 absorption. As shown in Fig. 8, the adsorption capacity could be considered to reach

10 equilibrium as the variation was in appreciable after 8 hours.



1

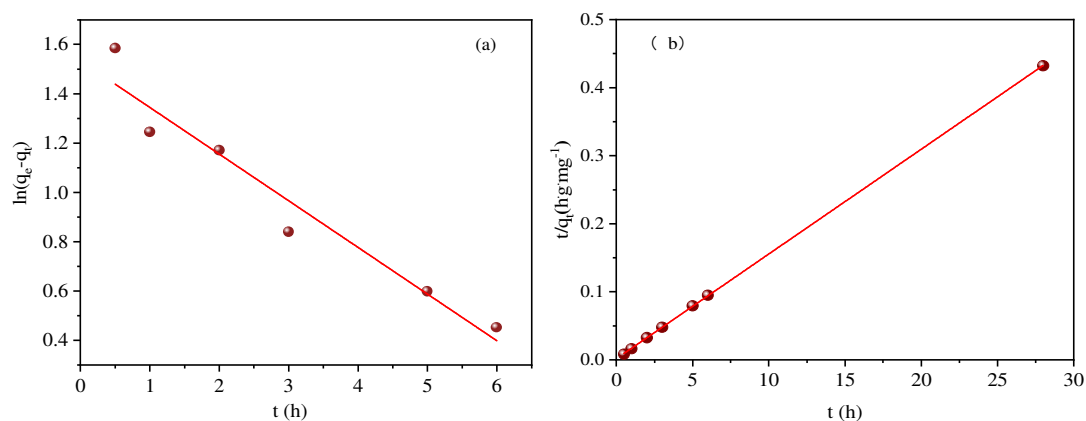
2 **Fig 8.** The effect of contact time on the adsorption capacity ( $q$ ) of CR (reaction  
 3 conditions:  $[\text{dye}] = 0.1 \text{ g}\cdot\text{L}^{-1}$ ,  $[\text{adsorbent}] = 0.05 \text{ g}$ ,  $T = 298 \text{ K}$ ,  $\text{pH} = 3.0$ ).

4 To make the results of adsorption kinetics clearer, the pseudo-first-order and  
 5 pseudo-second-order kinetic equations were applied to analyze the adsorption  
 6 mechanism, which expressed by equations (3) and (4), respectively. The Fig. 9 and  
 7 Table 1 was the statistical results which were well-fitted with pseudo-second-order  
 8 correlation. It means that the adsorption was mainly controlled by the chem-sorption  
 9 mechanism of  $\text{MnFe}_2\text{O}_4@\text{Cell-g-p(AA-DMC)}$  for CR dyes.

10 
$$\log(q_e - q_t) = \log q_e - \frac{k_1}{2.303} \cdot t \quad (3)$$

11 
$$\frac{t}{q_t} = \frac{1}{k_2 q_e^2} + \frac{t}{q_e} \quad (4)$$

12 Where,  $q_t \text{ (mg}\cdot\text{g}^{-1})$  and  $q_e \text{ (mg}\cdot\text{g}^{-1})$  were the adsorption capacity at given time  $t \text{ (h)}$   
 13 and the equilibrium adsorption capacity, respectively.  $k_1$  and  $k_2 \text{ (g}\cdot\text{mg}^{-1}\cdot\text{h}^{-1})$  were the  
 14 pseudo-first order rate constant and the pseudo-second order rate constant,  
 15 respectively (Luo et al. 2013).



1

2 **Fig 9.** Pseudo-first-order (a) and pseudo-second-order (b) kinetics of CR adsorption  
 3 on  $\text{MnFe}_2\text{O}_4@\text{Cel-g-p}(\text{AA-DMC})$ . (reaction conditions:  $[\text{dye}] = 0.1 \text{ g}\cdot\text{L}^{-1}$ ,  $[\text{adsorbent}]$   
 4  $= 0.05 \text{ g}$ ,  $T = 298 \text{ K}$ ,  $\text{pH} = 3.0$ ).

5 **Table 1.** The parameters of the kinetics of  $\text{MnFe}_2\text{O}_4@\text{Cel-g-p}(\text{AA-DMC})$  for CR dye.

Pseudo-first-order model		Pseudo-second-order model	
$k_1$	0.4357	$k_2$	0.1444
$R^2$	0.94507	$R^2$	0.99998

### 6 3.2.3 Adsorption isotherms

7 The adsorption experiments of CR were performed in the initial dye  
 8 concentration range of  $100\text{-}600 \text{ mg}\cdot\text{L}^{-1}$  at room temperature. The relevant adsorption  
 9 parameters were analyzed fitting to the Langmuir and Freundlich isotherm models  
 10 denoted by eqs (5) and (6). The adsorption isotherms curves of CR of Fig. 10 and  
 11 Table 2 presented the inter-related parameters of the two isotherm models. The results  
 12 reflected that the Freundlich model possessed a higher correlation coefficient so that  
 13 this work could be applied for non-ideal adsorption on multi-layer adsorption.

14 
$$\frac{C_e}{q_e} = \frac{1}{q_{\max} \cdot K_L} + \frac{C_e}{q_{\max}}$$

15 (5)

$$\ln q_e = \ln K_F + \frac{1}{n} \ln C_e \quad (6)$$

Where,  $K_L$  ( $L \cdot mg^{-1}$ ) meant the Langmuir constant,  $K_F$  and  $n$  value were the Freundlich constant and the adsorption intensity, respectively.  $C_e$  ( $mg \cdot L^{-1}$ ) was the dye concentration at equilibrium.  $q_e$ ,  $q_{max}$  were the adsorption capacity at equilibrium and the maximum adsorption capacity of CR adsorbed on  $MnFe_2O_4@Cel-g-p(AA-DMC)$  (Alekseeva et al. 2017).

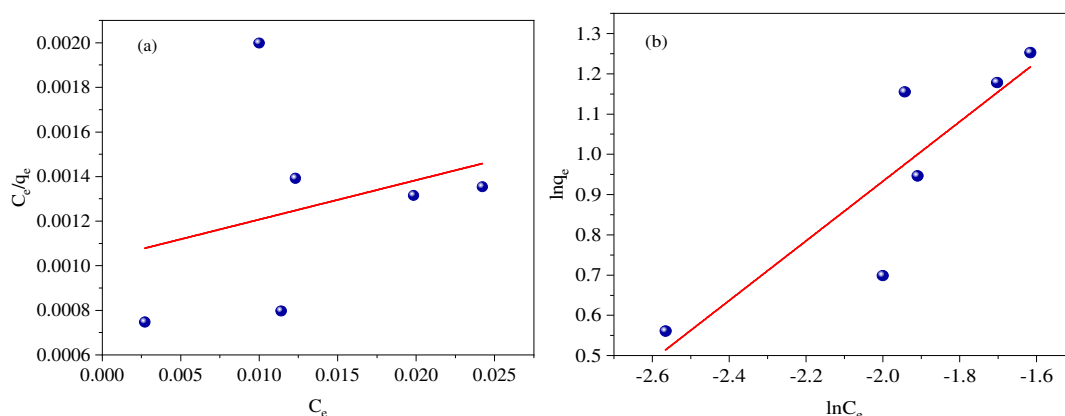


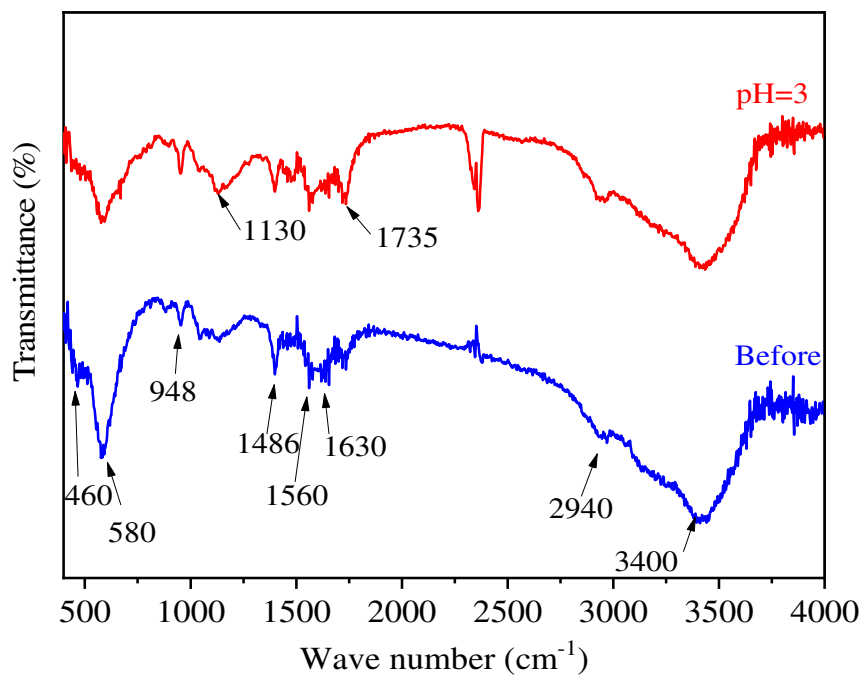
**Fig 10.** Langmuir (a) and Freundlich (b) isotherm curves of CR adsorption on  $MnFe_2O_4@Cel-g-p(AA-DMC)$ . (reaction conditions: [adsorbent]=0.05 g, T=298 K, pH=3.0).

**Table 2.** Isotherm parameters of  $MnFe_2O_4@Cel-g-p(AA-DMC)$  for CR dye.

Langmuir model		Freundlich model	
$q_{max}(mg \cdot g^{-1})$	56.6251	$1/n$	0.7406
$K_L (L \cdot mg^{-1})$	17.1456	$K_F$	11.1804
$R^2$	0.0858	$R^2$	0.7643

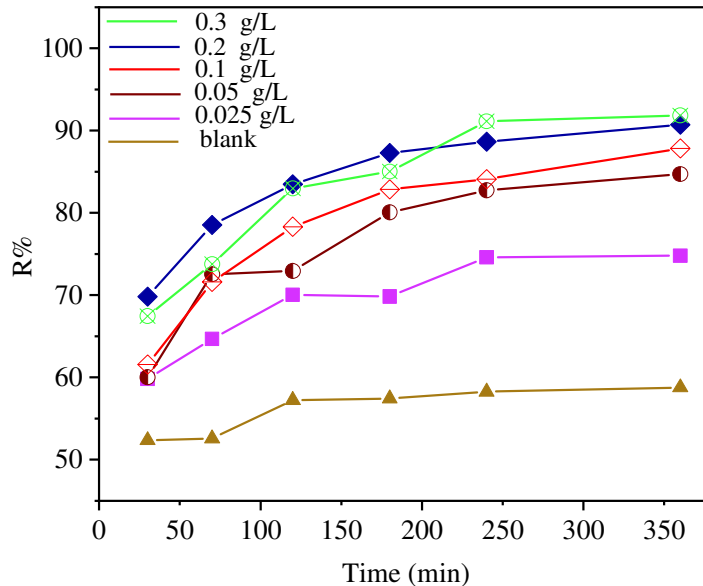
Fig. 11 illustrated the FT-IR spectrum analysis of the  $MnFe_2O_4@Cel-g-p(AA-DMC)$  before and after adsorption of the Congo red dye. The stretching vibration peaks at  $460 \text{ cm}^{-1}$  (Mn-O) and  $580 \text{ cm}^{-1}$  (Fe-O) were mainly due to the formation of metal covalent bonds at octahedral and tetrahedral sites of the

1 spinel structure (Wang et al. 2020; Zhou et al. 2020). The results indicated the  
2 presence of  $\text{MnFe}_2\text{O}_4$  in the adsorbents. The peaks at  $3400\text{ cm}^{-1}$  and  $2940\text{ cm}^{-1}$  were in  
3 accordance with hydrogen bonds (-OH) stretching vibration and C-H ( $\text{CH}_3$ )  
4 antisymmetric stretching vibration of saturated hydrocarbon in cellulose, respectively.  
5 The characteristic peaks of modified cellulose were observed including  $948\text{ cm}^{-1}$   
6 (stretching vibration of quaternary ammonium),  $1130\text{ cm}^{-1}$  (asymmetrical stretching  
7 vibration of C-O-C),  $1486\text{ cm}^{-1}$  (bending vibration of  $-\text{CH}_2-\text{N}^+(\text{CH}_3)_3$  group of DMC),  
8  $1560\text{ cm}^{-1}$  [vibration of tertiary amine (C-N)],  $1630\text{ cm}^{-1}$  [stretching vibration of C=C],  
9  $1735\text{ cm}^{-1}$  [stretching vibration of esterified linkage]. The above results verified that  
10 the cellulose was successfully grafted with AA and DMC (Wang et al. 2019; Tian et al.  
11 2012). Even more to the point, the peaks at  $1130\text{ cm}^{-1}$  and  $1735\text{ cm}^{-1}$  occurred slight  
12 enhancement on account of electrostatic attraction between adsorbents and CR dyes  
13 (Lu et al., 2019).



14  
15 **Fig 11.** FT-IR spectra of the  $\text{MnFe}_2\text{O}_4@ \text{Cel-g-p(AA-DMC)}$  before and after CR  
16 adsorption.

1 Fig. 12 proved the effect of catalyst and catalyst concentration on the removal  
 2 efficiency of CR dyes. There was no catalyst in the reaction system, the removal  
 3 efficiency of Congo red was only 58.7%. Once added the PMS, the removal  
 4 efficiency was significantly increased, reaching the highest value of 74.6%. At the  
 5 same time, the faster the catalytic rate increased, the higher the removal efficiency of  
 6 dye achieved. That was because PMS could be activated by the transition metal (such  
 7 as Fe, Mn, Co and so on) to produce sulfate ions, which could interact with organic  
 8 dyes, so as to achieve the purpose of degradation of dyes. When the concentration of  
 9 PMS reached  $0.2 \text{ g}\cdot\text{L}^{-1}$ , the removal efficiency reached 90.7%. Even if the  
 10 concentration of PMS continued to rise, the removal efficiency did not change  
 11 significantly, indicating that the adsorbent had achieved saturation (Ghanbari et al.  
 12 2019).

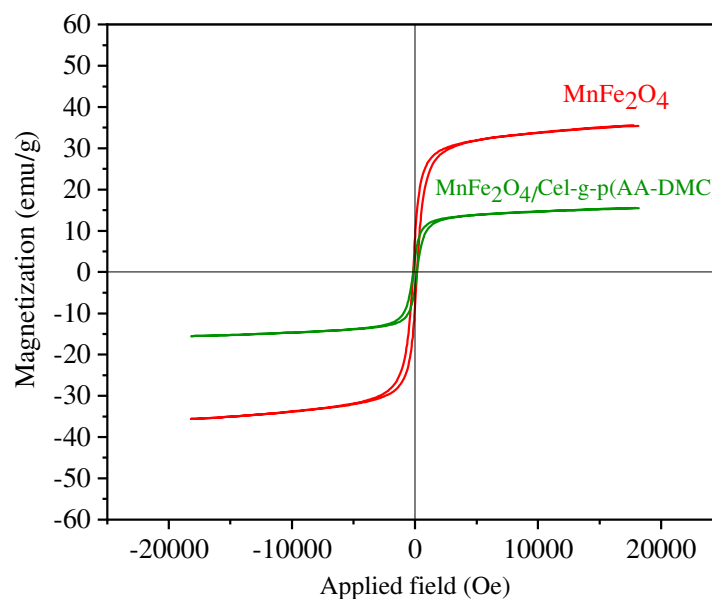


13  
 14 **Fig 12.** The effect of catalyst dosage on the removal efficiency (R%) of CR (reaction  
 15 conditions: [dye]= $0.08 \text{ g}\cdot\text{L}^{-1}$ , [adsorbent]= $0.05 \text{ g}$ ,  $T=298 \text{ K}$ ,  $\text{pH}=3.0$ ).

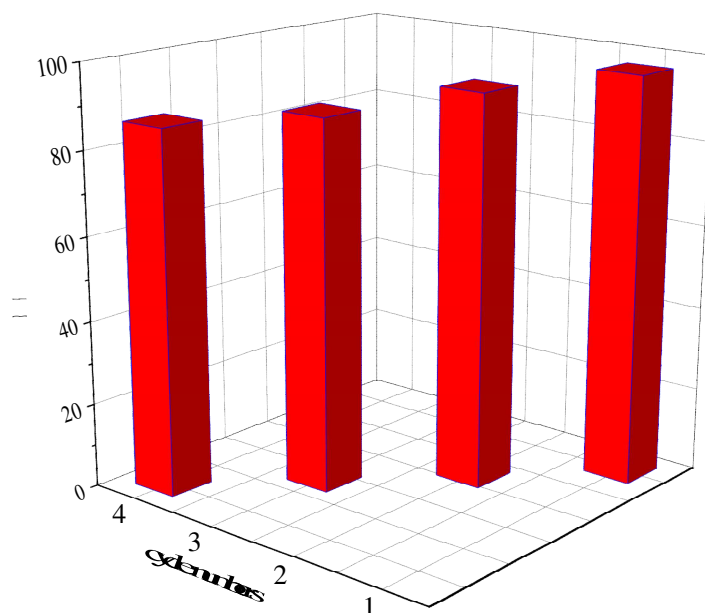
### 16 3.3 Stability and Reusability

17 The magnetic behavior of the  $\text{MnFe}_2\text{O}_4$  and  $\text{MnFe}_2\text{O}_4@\text{Cel-g-p(AA-DMC)}$  were

1 evaluated by VSM curves. In Fig. 13, the saturation magnetization ( $M_s$ ) values of the  
2  $MnFe_2O_4$  and  $MnFe_2O_4@Cel-g-p(AA-DMC)$  were 35.44 and 12.89  $emu \cdot g^{-1}$  at 18155  
3 and 18173 Oe, respectively (Mady et al. 2019). No doubt the saturation magnetization  
4 value decreased relatively along with the composition of the non-magnetic modified  
5 cellulose (Amoli-Diva et al. 2019). Meanwhile, the magnetic coercivity ( $H_c$ ) were  
6 7.8111 and 15.6069 Oe, respectively. The remanences ( $M_R$ ) were 0.634 and 0.237  
7  $emu \cdot g^{-1}$ , respectively. Due to paramagnetic behavior, these results exhibited long-term  
8 reusability and stability of  $MnFe_2O_4@Cel-g-p(AA-DMC)$  for congo dyes (Mady et al.  
9 2019). As shown in inset image, the adsorbents possessed the ability for magnetic  
10 manipulation (Ma et al. 2019).



11  
12 **Fig 13.** Magnetization property of the  $MnFe_2O_4$  and  $MnFe_2O_4@Cel-g-p(AA-DMC)$ ,  
13 inset image of  $MnFe_2O_4@Cel-g-p(AA-DMC)$  dispersed in wastewater and separated  
14 from wastewater under an external magnetic field.



1

2 **Fig 14.** Removal efficiency of MnFe<sub>2</sub>O<sub>4</sub>@Cel-g-p(AA-DMC) with multiple cycles of  
 3 regeneration. (reaction conditions: [dye]=0.08 g.L<sup>-1</sup>, [adsorbent]=0.05 g, T=298 K,  
 4 pH=3.0).

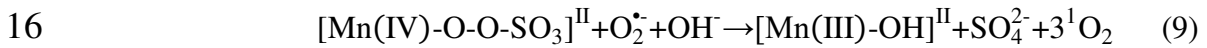
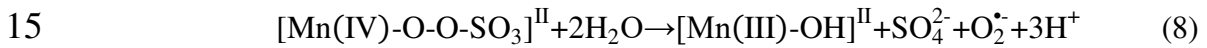
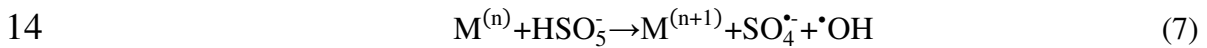
5 The catalytic stability and recyclability of the MnFe<sub>2</sub>O<sub>4</sub>@Cel-g-p(AA-DMC)  
 6 were evaluated from successive catalytic experiments. Four-run recyclability tests  
 7 were carried out in this work in Fig. 14. It was clearly found that the removal rate of  
 8 CR via PMS activated by MnFe<sub>2</sub>O<sub>4</sub> decreased from 96.9% (first cycle) to 93.5%  
 9 (second cycle) and 86.6% (fourth cycle). The removal efficiency of CR in the  
 10 retrievable experiment was decreased due to the reduction of adsorption sites, which  
 11 was possibly due to the production of the reaction intermediates covering on the  
 12 surface of the adsorbent. In a word, the prepared adsorbents were steady after four  
 13 cycles.

#### 14 3.4 Reaction Mechanism

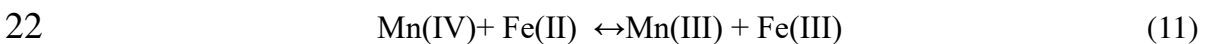
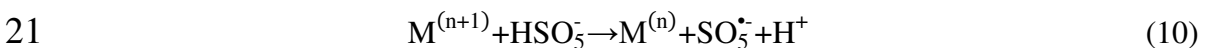
15 Possible mechanism diagram of MnFe<sub>2</sub>O<sub>4</sub>@Cel-g-p(AA-DMC)/PMS system for  
 16 the adsorption of Congo red dye were shown in Fig. 15. The pH experiment proved  
 17 that cellulose modified by cationic polymers generated electrostatic attraction with the

1 anionic Congo red dye in acidic environment, which greatly shortened the  
 2 intermolecular distance between adsorbents and CR dyes, thus improving the  
 3 adsorption efficiency of the Congo red dyes.

4 Meanwhile, it also had the function of degrading CR dyes via activating the PMS  
 5 to get ROS. According to relevant reports the activation mechanism of PMS was  
 6 speculated as follows. The exposed Mn sites on the adsorbents was the dominating  
 7 catalytic centers for PMS activation. Generally, the PMS activation mainly occurred  
 8 on the surface of MnFe<sub>2</sub>O<sub>4</sub>@Cel-g-p(AA-DMC), along with redox cycles of metals  
 9 and the production of reactive radicals (Du et al. 2019). As elucidated in  
 10 eqs.7-12, HSO<sub>5</sub><sup>-</sup> firstly combined with metal oxides via electrostatic attraction or  
 11 OH-mediated coaction (eq.7) (Yao et al. 2014). Subsequently, the adsorbent surface  
 12 metastable manganese intermediate (Mn(IV)-O-O-SO<sub>3</sub>) generated O<sub>2</sub><sup>•-</sup> and <sup>1</sup>O<sub>2</sub>  
 13 under the surrounding liquid (eqs.8, 9) (Wang et al. 2014).

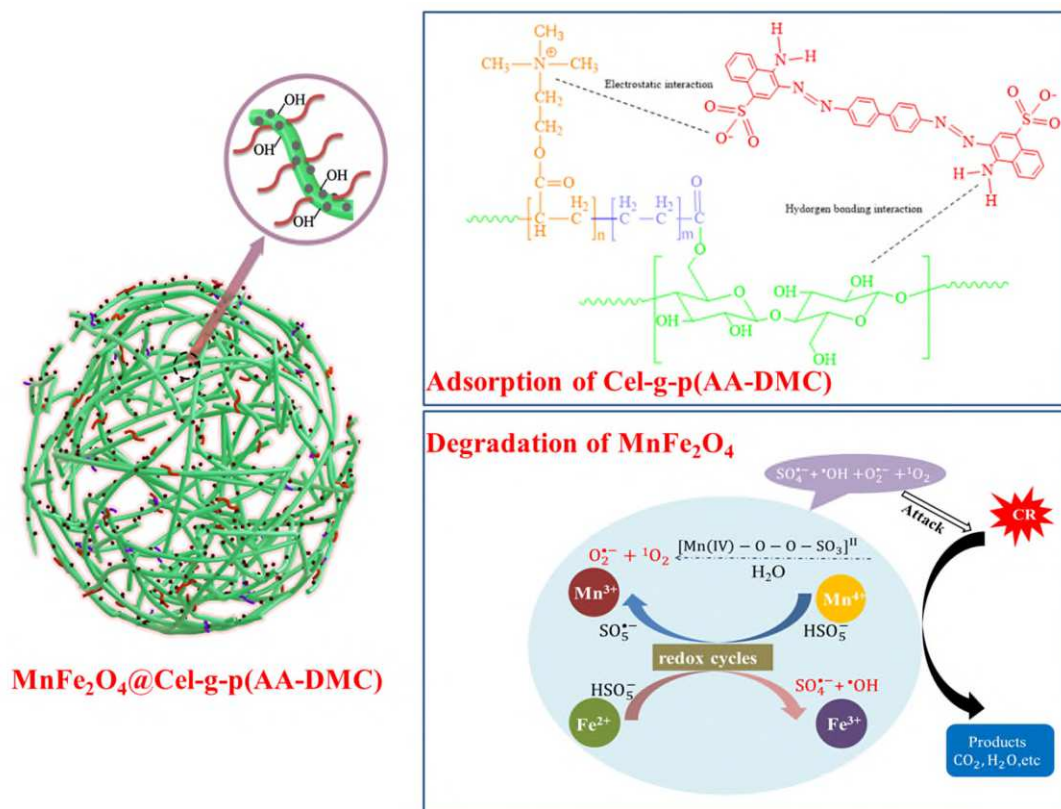


17 Moreover, the reduction of metals by HSO<sub>5</sub><sup>-</sup> produced SO<sub>5</sub><sup>•-</sup> as a radical  
 18 byproduct (eq.10). The reaction was benefited by redox cycles of metal Mn and Fe  
 19 (eq.11). Finally, the various ROS played an important role in degrading organic dyes  
 20 tuffs to facilitate the efficient removal of CR (eq.12) (Wang et al. 2014).



24 To sum up, magnetic MnFe<sub>2</sub>O<sub>4</sub> nanoparticles via the activation of PMS could

1 degrade CR dyes and cellulose grafted with poly(AA-DMC) played an important role  
 2 in chemical adsorption. The CR dyes were successfully removed under the synergistic  
 3 action of chemical degradation and adsorption.



4  
 5 **Fig 15.** Possible mechanism diagram of MnFe<sub>2</sub>O<sub>4</sub>@Cel-g-p(AA-DMC)/PMS system  
 6 for the adsorption of Congo red dye.

7 **4. Conclusion**

8 In this work, a new green adsorbent was successfully synthesized by a facile  
 9 co-precipitation method, in which cellulose grafted with poly(AA-DMC) was  
 10 crosslinked with magnetic MnFe<sub>2</sub>O<sub>4</sub> nanoparticles in the presence of crosslinking  
 11 agent, to serve as adsorbent for CR dyestuff. Not only could it be applied to  
 12 Fenton-like advanced oxidation systems, PMS catalysis, according to cycling  
 13 experiments, the MnFe<sub>2</sub>O<sub>4</sub>@Cel-g-p(AA-DMC) was also found to be reused multiple  
 14 times (R% decreased about 9%, from 96.91 % to 86.57%) under the external magnetic

1 fields. The used conditions of adsorbents were investigated and the optimum value of  
2 pH was 3, the optimum concentration for PMS is  $0.2 \text{ g}\cdot\text{L}^{-1}$  and the maximum  
3 adsorption capacity was  $73.48 \text{ mg}\cdot\text{g}^{-1}$ . The kinetic data of the adsorbent were fitted to  
4 the pseudo-second-order model, and the adsorption data were matched with the  
5 Frenudlich isotherm model. Furthermore, possible mechanism was investigated, ROS  
6 generated by activation of PMS played a degradation role and the modified cellulose  
7 adsorbed CR via electrostatic attraction. Furthermore,  $\text{MnFe}_2\text{O}_4@\text{Cel-g-p}(\text{AA-DMC})$   
8 was characterized by SEM, TEM, XPS, XRD, BET, VSM, TGA and FTIR. Thus, it is  
9 expected that the adsorbent display strong potential for the removal of CR dyes from  
10 organic wastewater.

11

## 12 **Acknowledgments**

13 The authors greatly acknowledge the financial support provided by the National  
14 Natural Science Foundation of China (21671026), the Hunan Provincial Natural  
15 Science Foundation of China (2019JJ40310), Research Fund of Science and  
16 Technology Innovation Platform of Key Laboratory of Dongting Lake Aquatic  
17 Eco-Environmental Control and Restoration of Hunan Province (2020DT008), Project  
18 of Changsha City Science and Technology Bureau (kq2004064).

19

## 20 **References**

21 Sanna H, Amit B, Mika S (2016) A review on modification methods to  
22 cellulose-based adsorbents to improve adsorption capacity. *Water Res.* 91, 156-173.  
23 Anjum M, Miandad R, Waqas M, Gehany F, Barakat M (2019) Remediation of  
24 wastewater using various nano-materials. *Arab. J. Chem.* 12 (8), 4897-4919.

1 Malatji N, Makhado E, Ramohlola K. E, Modibane K. D, Maponya T. C, Monama G.  
2 R, Hato M. J (2020) Synthesis and characterization of magnetic clay-based  
3 carboxymethyl cellulose-acrylic acid hydrogel nanocomposite for methylene blue dye  
4 removal from aqueous solution. *Environ. Sci. Pollut. Res. Int.* 27 (35), 44089- 44105.

5 Chaudhary, G. R., Saharan, P, Kumar A, Mehta S. K, Mor S, Umar A (2013)  
6 Adsorption studies of cationic, anionic and azo-dyes via monodispersed Fe<sub>3</sub>O<sub>4</sub>  
7 nanoparticles. *J. Nanosci. Nanotechnol.* 13 (5), 3240-3245.

8 Kamel S, El-Gendy A. A, Hassan M. A, El-Sakhawy M, Kelnar I (2020)  
9 Carboxymethyl cellulose-hydrogel embedded with modified magnetite nanoparticles  
10 and porous carbon: Effective environmental adsorbent. *Carbohydr. Polym.* 242,  
11 116402.

12 An Y, Zheng H, Sun Q, Zheng X, Wu Q, Zhao R (2019) A novel floating adsorbents  
13 system of acid orange 7 removal: Polymer grafting effect. *Sep. Purif. Technol.* 227.

14 Moharrami P, Motamedi E (2020) Application of cellulose nanocrystals prepared from  
15 agricultural wastes for synthesis of starch-based hydrogel nanocomposites: Efficient  
16 and selective nanoadsorbent for removal of cationic dyes from water. *Bioresour*  
17 *Technol.* 313, 123661.

18 Zhang J, Cui F, Xu L, Ma Q, Gao Y, Liu Y, Cui T (2020) Construction of magnetic  
19 NiO/C nanosheets derived from coordination polymers for extraordinary adsorption  
20 of dyes. *J. Colloid. Interface. Sci.* 561, 542-550.

21 Liu H, Yang X, Zhang Y, Zhu H, Yao J (2014) Flocculation characteristics of  
22 polyacrylamide grafted cellulose from *Phyllostachys heterocycla*: An efficient and  
23 eco-friendly flocculant. *Water Res.* 59, 165-171.

24 Shi C, Zhang L, Bian H, Shi Z, Ma J, Wang Z (2021) Construction of

1 Ag-ZnO/cellulose nanocomposites via tunable cellulose size for improving  
2 photocatalytic performance. *J. Clean. Prod.* 288,125089.

3 Jiang X, Lou C, Hua F, Deng H, Tian X (2020) Cellulose nanocrystals-based  
4 flocculants for high-speed and highefficiency decolorization of colored effluents. *J.*  
5 *Clean. Prod.* 251, 119749.

6 Wang Z, Huang W, Yang G, Liu Y, Liu S (2019) Preparation of cellulose-base  
7 amphoteric flocculant and its application in the treatment of wastewater. *Carbohydr.*  
8 *Polym.* 215, 179-188.

9 An X, Cheng D, Dai L, Wang B, Ocampo H. J, Nasrallah J, Jia X, Zou J, Long Y, Ni  
10 Y (2017) Synthesis of nano-fibrillated cellulose/magnetite/titanium dioxide  
11 (NFC@Fe<sub>3</sub>O<sub>4</sub>@TNP) nanocomposites and their application in the photocatalytic  
12 hydrogen generation. *Appl. Catal. B: Environ.* 206, 53-64.

13 Amiralian N, Mustapic M, Hossain M. S. A, Wang C, Konarova M, Tang J, Na J,  
14 Khan A, Rowan A (2020) Magnetic nanocellulose: A potential material for removal of  
15 dye from water. *J. Hazard. Mater.* 394,122571.

16 Arabkhani P, Asfaram A (2020) Development of a novel three-dimensional magnetic  
17 polymer aerogel as an efficient adsorbent for malachite green removal. *J. Hazard.*  
18 *Mater.* 384,121394.

19 Li M, Liu H, Chen T, Chen D, Wang C, Wei L, Wang L (2020) Efficient U(VI)  
20 adsorption on iron/carbon composites derived from the coupling of cellulose with iron  
21 oxides: Performance and mechanism. *Sci. Total. Environ.* 703, 135604.

22 Chen X, Cui J, Xu X, Sun B, Zhang L, Dong W, Chen C, Sun D (2020) Bacterial  
23 cellulose/attapulgitic magnetic composites as an efficient adsorbent for heavy metal  
24 ions and dye treatment. *Carbohydr. Polym.* 29,115512.

1 Alekseeva O. V, Rodionova A. N, Bagrovskaya N. A, Agafonov A. V, Noskov A. V  
2 (2017) Hydroxyethyl cellulose/bentonite/magnetite hybrid materials: structure,  
3 physicochemical properties, and antifungal activity. *Cellulose*, 24 (4), 1825- 1836.

4 Tian X, Ren E, Wang J, Zou J, Tao Y, Wang S, Jiang X (2012) Synthesis and  
5 flocculation property in dye solutions of  $\beta$ -cyclodextrin–acrylic acid–  
6 [2-(Acryloyloxy)ethyl] trimethyl ammonium chloride copolymer. *Carbohydr. Polym.*  
7 87 (3), 1956-1962.

8 Lu H, Zhang L, Wang B, Long Y, Zhang M, Ma J, Khan A, Chowdhury S. P, Zhou X,  
9 Ni Y (2019) Cellulose-supported magnetic  $\text{Fe}_3\text{O}_4$ –MOF composites for enhanced dye  
10 removal application. *Cellulose*, 26 (8), 4909-4920.

11 Kalantari E, Khalilzadeh M. A, Zareyee D, Shokouhimehr M (2020) Catalytic  
12 degradation of organic dyes using green synthesized  $\text{Fe}_3\text{O}_4$ -cellulose-copper  
13 nanocomposites. *J. Mol. Struct.* 1218,128488.

14 Pang Y, Lei H (2016) Degradation of p-nitrophenol through microwave-assisted  
15 heterogeneous activation of peroxymonosulfate by manganese ferrite. *Chem. Eng. J.*  
16 287, 585-592.

17 Qian H, Hou Q, Yu G, Nie Y, Bai C, Bai X, Ju M (2020) Enhanced removal of dye  
18 from wastewater by Fenton process activated by core-shell  $\text{NiCo}_2\text{O}_4$ @FePc catalyst. *J.*  
19 *Clean. Prod.* 273,123028.

20 Wang Z, Lai C, Qin L, Fu Y, He J, Huang D, Li B, Zhang M, Liu S, Li L, Zhang W, Yi  
21 H, Liu X, Zhou X (2020) ZIF-8-modified  $\text{MnFe}_2\text{O}_4$  with high crystallinity and  
22 superior photo-Fenton catalytic activity by Zn-O-Fe structure for TC degradation.  
23 *Chem. Eng. J.* 392,124851.

24 Mady A. H, Baynosa M. L, Tuma D, Shim J (2019) Heterogeneous activation of

1 peroxymonosulfate by a novel magnetic 3D  $\gamma$ -MnO<sub>2</sub>@ZnFe<sub>2</sub>O<sub>4</sub>/rGO nanohybrid as a  
2 robust catalyst for phenol degradation. *Appl. Catal. B: Environ.* 244, 946-956.

3 Zhou X, Kong L, Jing Z, Wang S, Lai Y, Xie M, Ma L, Feng Z, Zhan J (2020) Facile  
4 synthesis of superparamagnetic beta-CD-MnFe<sub>2</sub>O<sub>4</sub> as a peroxymonosulfate activator  
5 for efficient removal of 2,4-dichlorophenol: structure, performance, and mechanism. *J.*  
6 *Hazard. Mater.* 394, 122528.

7 Lops C, Ancona A, Di Cesare K, Dumontel B, Garino N, Canavese G, Hernandez S,  
8 Cauda V (2019) Sonophotocatalytic degradation mechanisms of Rhodamine B dye via  
9 radicals generation by micro- and nano-particles of ZnO. *Appl. Catal. B: Environ.* 243,  
10 629-640.

11 Wang Y, Sun H, Ang H. M, Tade M. O, Wang S (2014) Facile synthesis of  
12 hierarchically structured magnetic MnO<sub>2</sub>/ZnFe<sub>2</sub>O<sub>4</sub> hybrid materials and their  
13 performance in heterogeneous activation of peroxymonosulfate. *ACS. Appl. Mater.*  
14 *Interfaces*, 6 (22), 19914-19937.

15 Lu H, Zhang L, Ma J, Alam N, Zhou X, Ni Y (2019) Nano-Cellulose/MOF Derived  
16 Carbon Doped CuO/Fe<sub>3</sub>O<sub>4</sub> Nanocomposite as high efficient catalyst for organic  
17 pollutant remedy. *Nanomaterials (Basel)*. 9 (2), 277.

18 Yao Y, Cai Y, Lu F, Wei F, Wang X, Wang S (2014) Magnetic recoverable MnFe<sub>2</sub>O<sub>4</sub>  
19 and MnFe<sub>2</sub>O<sub>4</sub>-graphene hybrid as heterogeneous catalysts of peroxymonosulfate  
20 activation for efficient degradation of aqueous organic pollutants. *J. Hazard. Mater.*  
21 270, 61-70.

22 Zhao Y, Li Q, Ren H, Zhou R (2017) Activation of persulfate by magnetic  
23 MnFe<sub>2</sub>O<sub>4</sub>-bentonite for catalytic degradation of 2,4-dichlorophenol in aqueous  
24 solutions. *Chem. Res. Chinese U.* 33 (3), 415-421.

1 Desai H. B, Hathiya L. J, Joshi H. H, Tanna A. R (2020) Synthesis and  
2 characterization of photocatalytic  $\text{MnFe}_2\text{O}_4$  nanoparticles. Mater. Today, 21,  
3 1905-1910.

4 Pineda X, Quintana G. C, Herrera A. P, Sánchez J. H (2021) Preparation and  
5 characterization of magnetic cellulose fibers modified with cobalt ferrite nanoparticles.  
6 Mater. Chem. Phys. 259,122778.

7 Luo X, Zhang L, (2013) New solvents and functional materials prepared from  
8 cellulose solutions in alkali/urea aqueous system. Food Res. Int. 52 (1), 387- 400.

9 Zhou D, Zhang L, Guo S (2005) Mechanisms of lead biosorption on cellulose/chitin  
10 beads. Water Res. 39, 3755-3762.

11 Chen B, Zhao H, Chen S, Long F, Huang B, Yang B, Pan X (2019) A magnetically  
12 recyclable chitosan composite adsorbent functionalized with EDTA for simultaneous  
13 capture of anionic dye and heavy metals in complex wastewater. Chem. Eng. J. 356,  
14 69-80.

15 Chen Q, Zheng J, Yang Q, Dang Z, Zhang L (2019) Insights into the glyphosate  
16 adsorption behavior and mechanism by a  $\text{MnFe}_2\text{O}_4$ @Cellulose-Activated carbon  
17 magnetic hybrid. ACS. Appl. Mater. Interfaces. 11 (17), 15478-15488.

18 Huang X, Nan Z (2020) Synergetic adsorption and photo-Fenton degradation of  
19 methylene blue by  $\text{ZnFe}_2\text{O}_4/\text{SiO}_2$  magnetic double-mesoporous-shelled hollow  
20 spheres. Environ. Technol. 1-13,1725142.

21 Ghanbari F, Ahmadi M, Gohari F (2019) Heterogeneous activation of  
22 peroxymonosulfate via nanocomposite  $\text{CeO}_2\text{-Fe}_3\text{O}_4$  for organic pollutants removal:  
23 The effect of UV and US irradiation and application for real wastewater. Sep. Purif.  
24 Technol. 228,115732.

1 Sajjadi M, Nasrollahzadeh M, Tahsili M. R (2019) Catalytic and antimicrobial  
2 activities of magnetic nanoparticles supported N-heterocyclic palladium(II) complex:  
3 A magnetically recyclable catalyst for the treatment of environmental contaminants in  
4 aqueous media. *Sep. Purif. Technol.* 227,115716.

5 Wo, R., Li, Q.-L., Zhu, C., Zhang, Y., Qiao, G.-f., Lei, K.-y., Du, P., Jiang, W., 2019.  
6 Preparation and Characterization of Functionalized Metal–Organic Frameworks with  
7 Core/Shell Magnetic Particles ( $\text{Fe}_3\text{O}_4@ \text{SiO}_2@ \text{MOFs}$ ) for Removal of Congo Red and  
8 Methylene Blue from Water Solution. *J. Chem. Eng. Data*, 64 (6), 2455-2463.

9 Amoli-Diva M, Anvari A, Sadighi-Bonabi R (2019) Synthesis of  
10 magneto-plasmonic Au-Ag NPs-decorated  $\text{TiO}_2$ -modified  $\text{Fe}_3\text{O}_4$  nanocomposite with  
11 enhanced laser/solar-driven photocatalytic activity for degradation of dye pollutant in  
12 textile wastewater. *Ceram. Int.* 45 (14), 17837-17846.

13 Ma M, Yang Y, Li W, Ma Y, Tong Z, Huang W, Chen L, Wu G, Wang H, Lyu P (2019)  
14 Synthesis of yolk-shell structure  $\text{Fe}_3\text{O}_4/\text{P}(\text{MAA-MBAA})-\text{PPy}/\text{Au}/\text{void}/\text{TiO}_2$  magnetic  
15 microspheres as visible light active photocatalyst for degradation of organic pollutants.  
16 *J. Alloy. Comp.* 810,151807.

17 Du J, Bao J, Liu Y, Kim S. H, Dionysiou D. D (2019) Facile preparation of porous  
18  $\text{Mn}/\text{Fe}_3\text{O}_4$  cubes as peroxymonosulfate activating catalyst for effective bisphenol A  
19 degradation. *Chem. Eng. J.* 376,119193.

# Figures

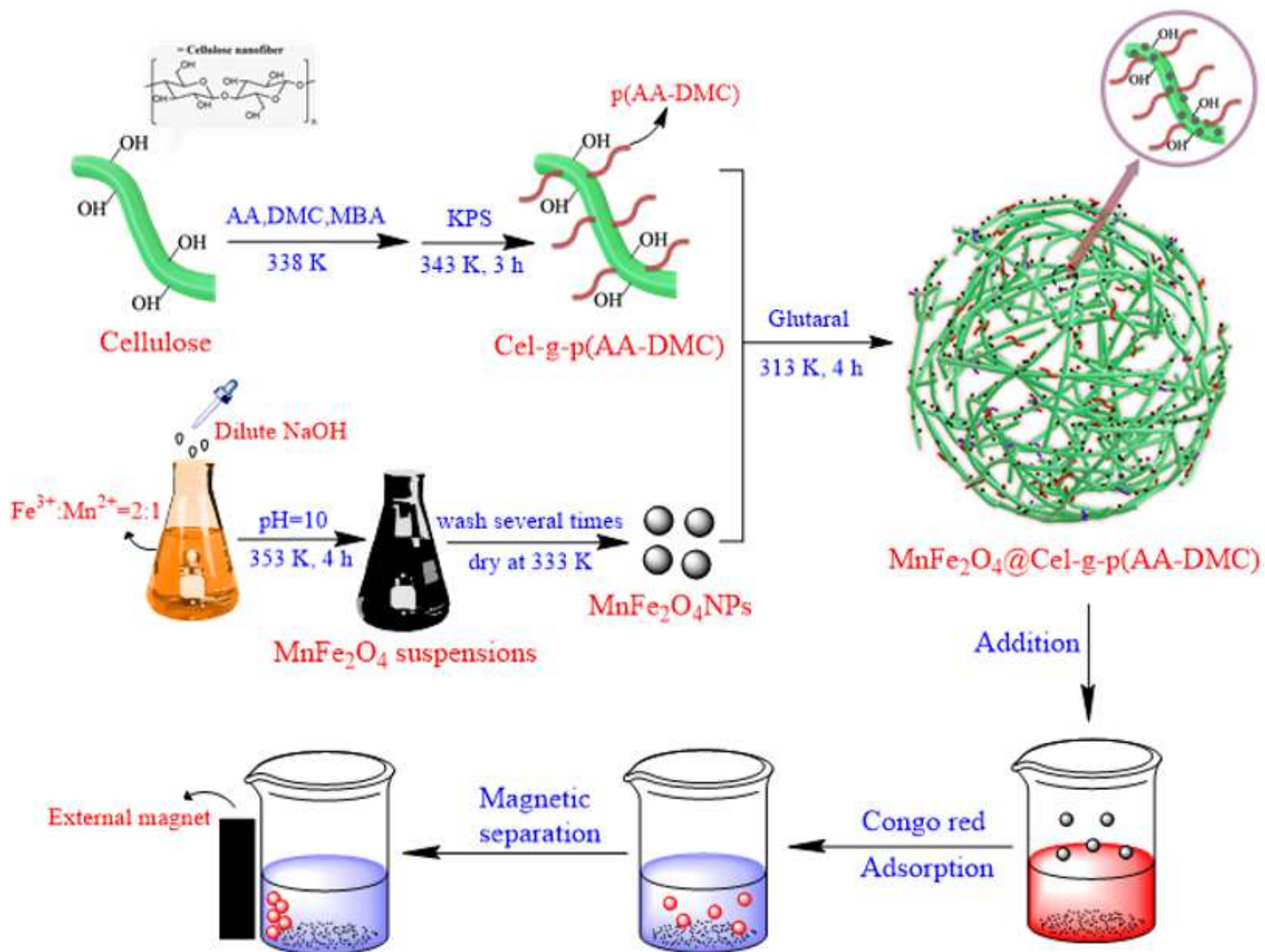
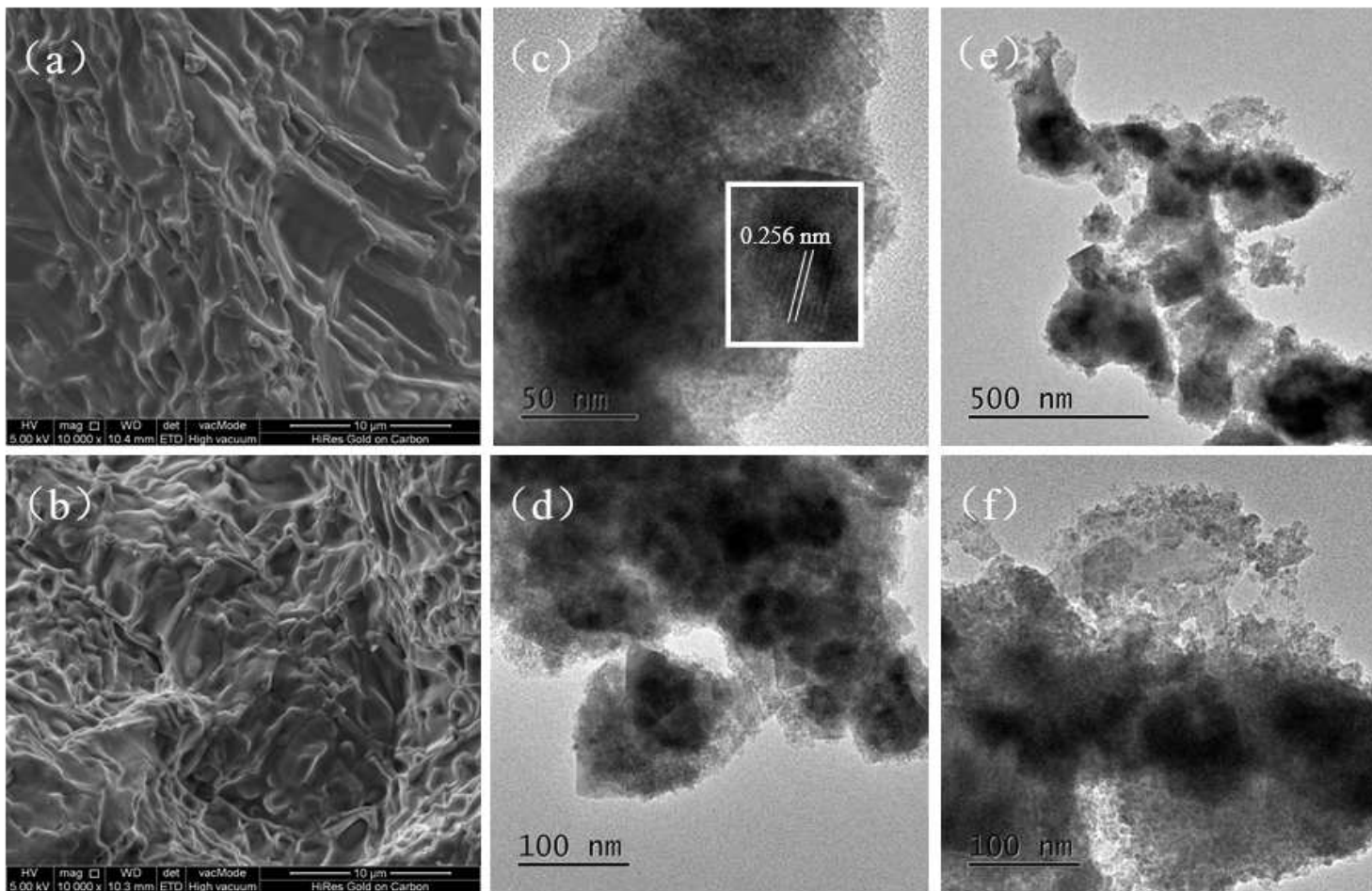


Figure 1

Schematic diagram of synthesis and adsorption of the MnFe<sub>2</sub>O<sub>4</sub>@Cel-g-p(AA-DMC) nanohybrid.



**Figure 2**

SEM images of Cel-g-p(AA-DMC) (a, b), HR-TEM images of MnFe<sub>2</sub>O<sub>4</sub> (c, d) and MnFe<sub>2</sub>O<sub>4</sub>@Cel-g-p(AA-DMC) (e, f).

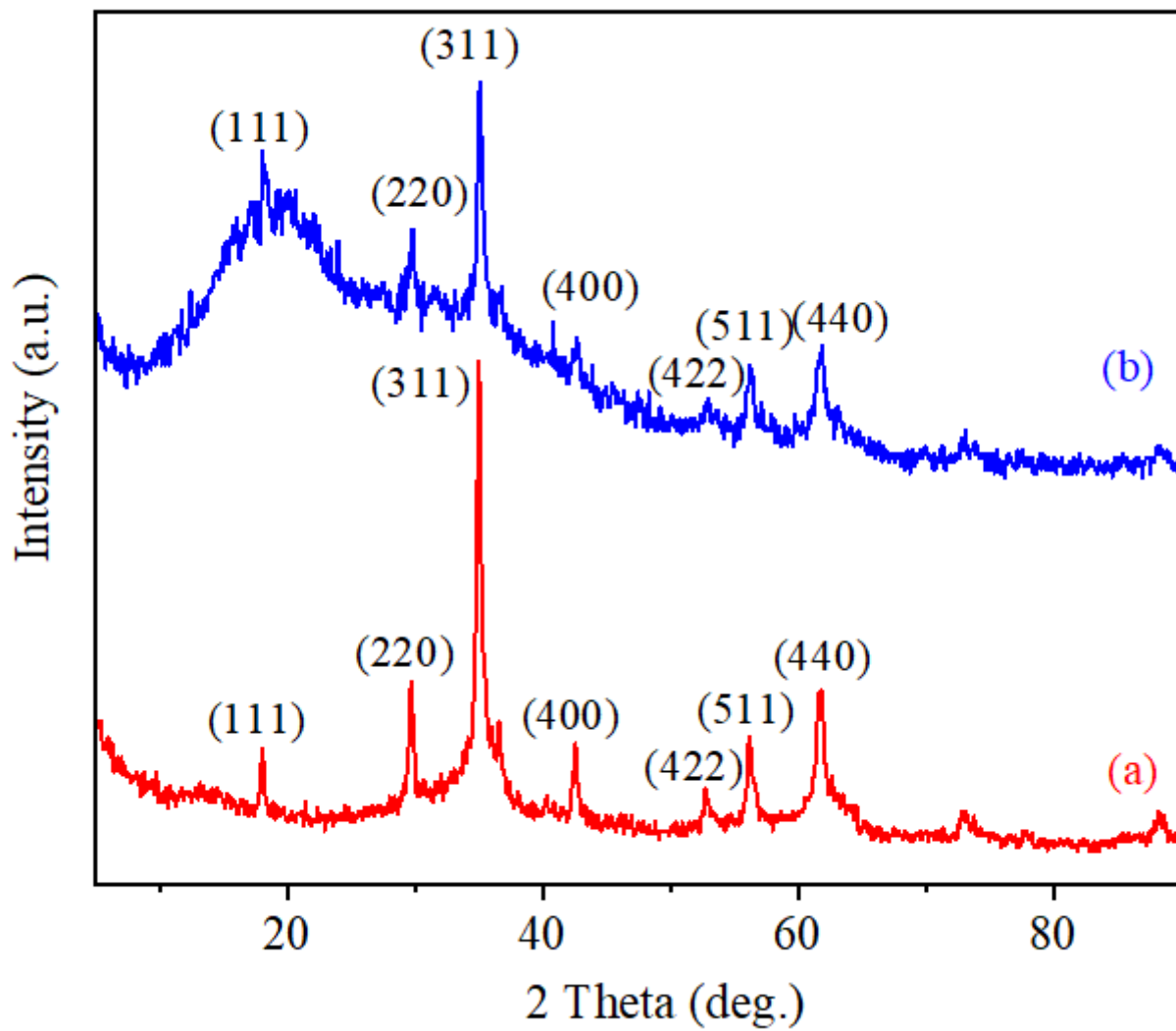


**Figure 3**

XRD pattern of  $\text{MnFe}_2\text{O}_4$  (a),  $\text{MnFe}_2\text{O}_4@$ Cel-g-p(AA-DMC) (b).

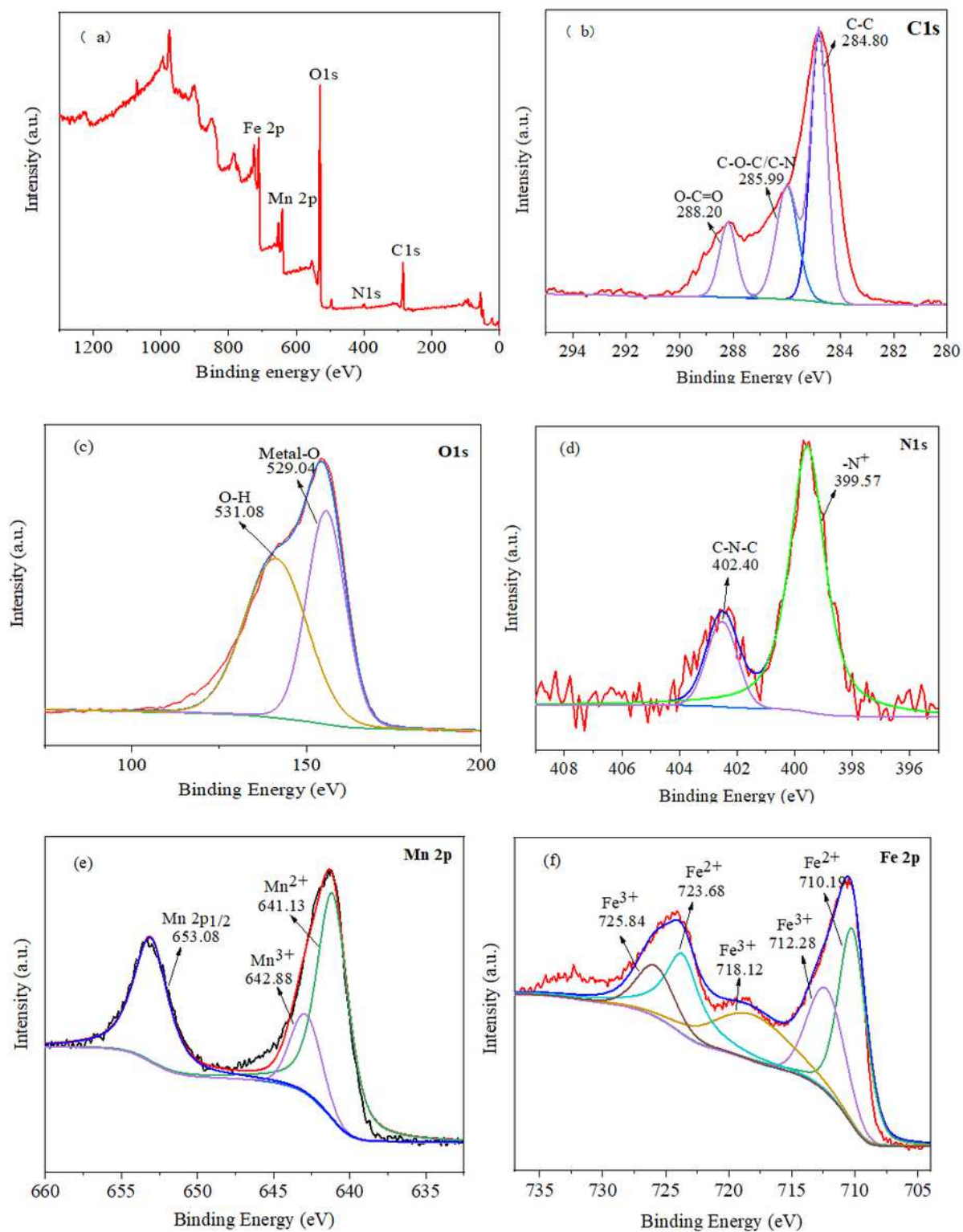


**Figure 4**

XPS survey (a), C1s (b), O1s (c), N1s (d), Mn 2p (e) and Fe 2p (f) spectra of MnFe<sub>2</sub>O<sub>4</sub>@Cel-g-p(AA-DMC).

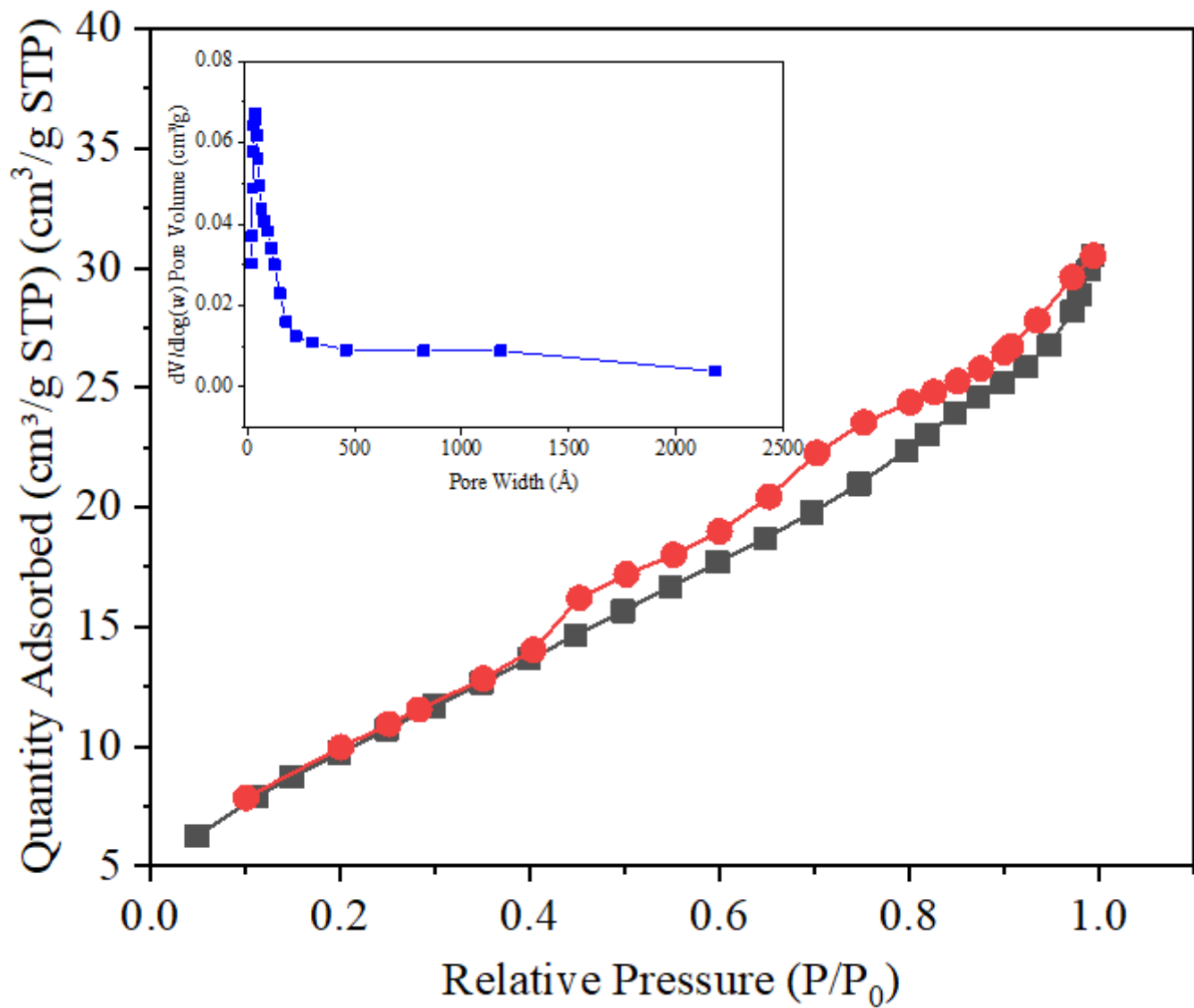


Figure 5

Nitrogen adsorption–desorption isotherms and the BJH pore size distributions of MnFe<sub>2</sub>O<sub>4</sub>@Cel-g-p(AA-DMC).

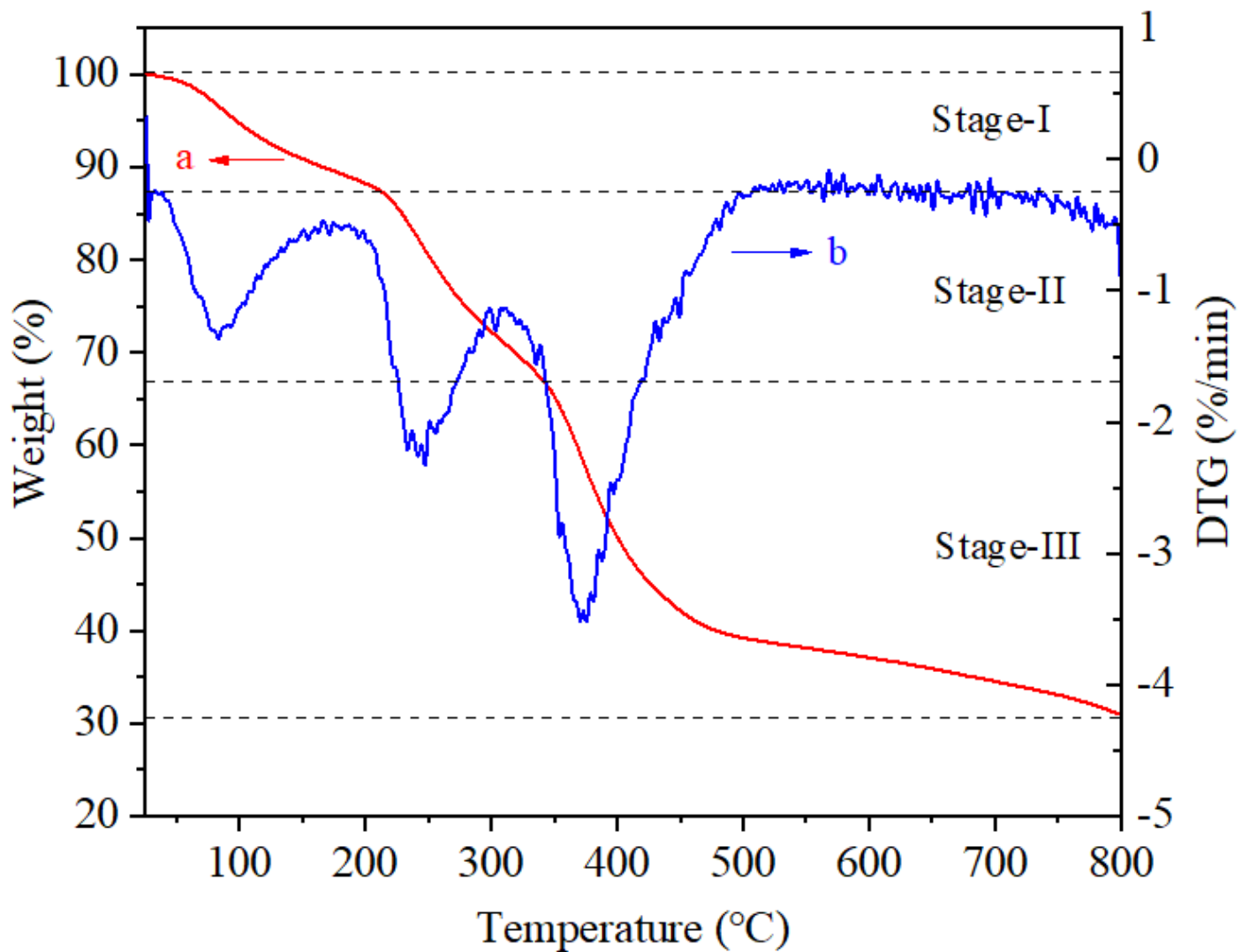
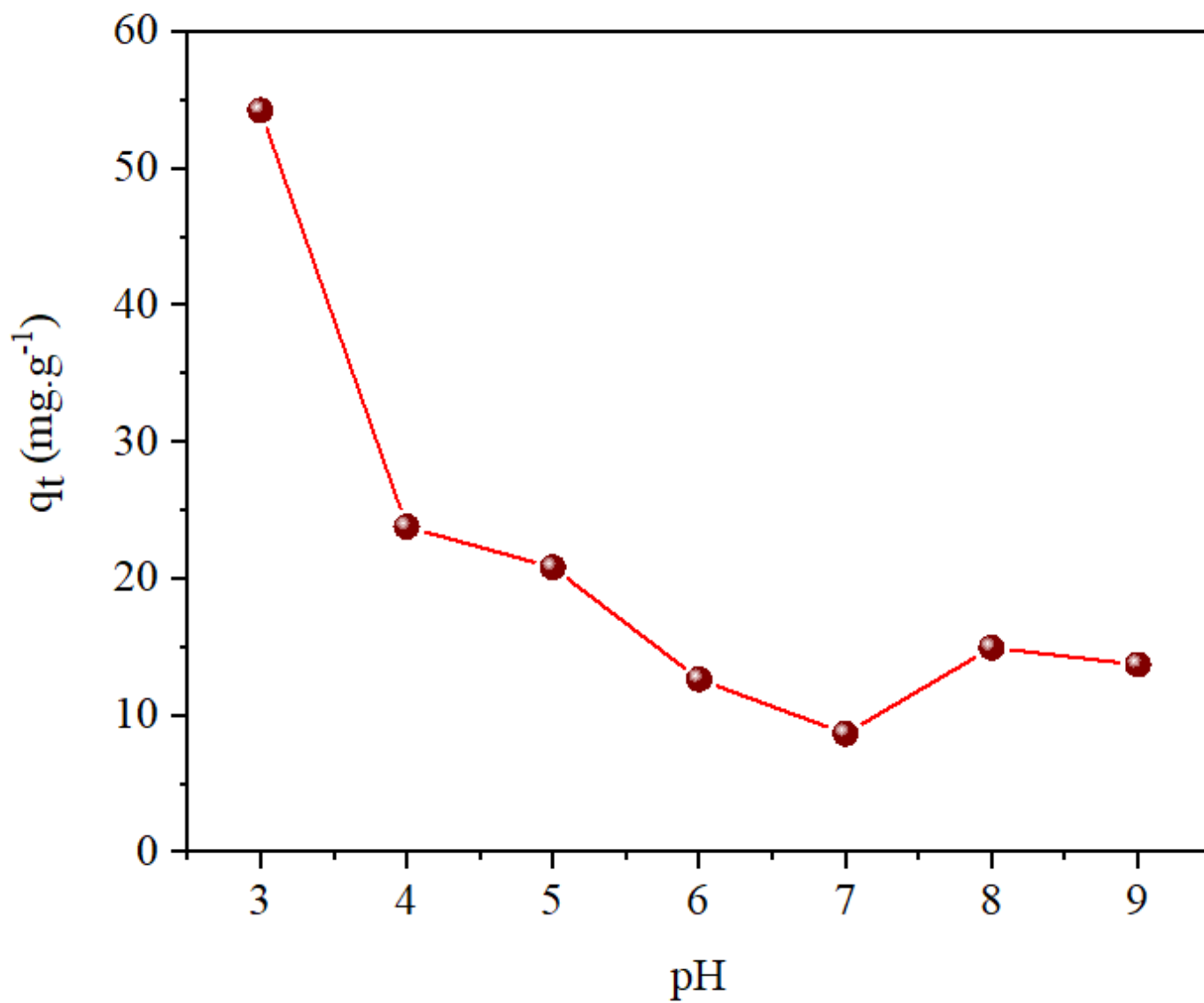


Figure 6

TG-DTG curve of the MnFe<sub>2</sub>O<sub>4</sub>@Cel-g-p(AA-DMC).



**Figure 7**

The effect of pH on the adsorption capacity ( $q_t$ ) of CR (reaction conditions:  $[\text{dye}] = 0.08 \text{ g}\cdot\text{L}^{-1}$ ,  $[\text{adsorbent}] = 0.05 \text{ g}$ ,  $T = 298 \text{ K}$ ).

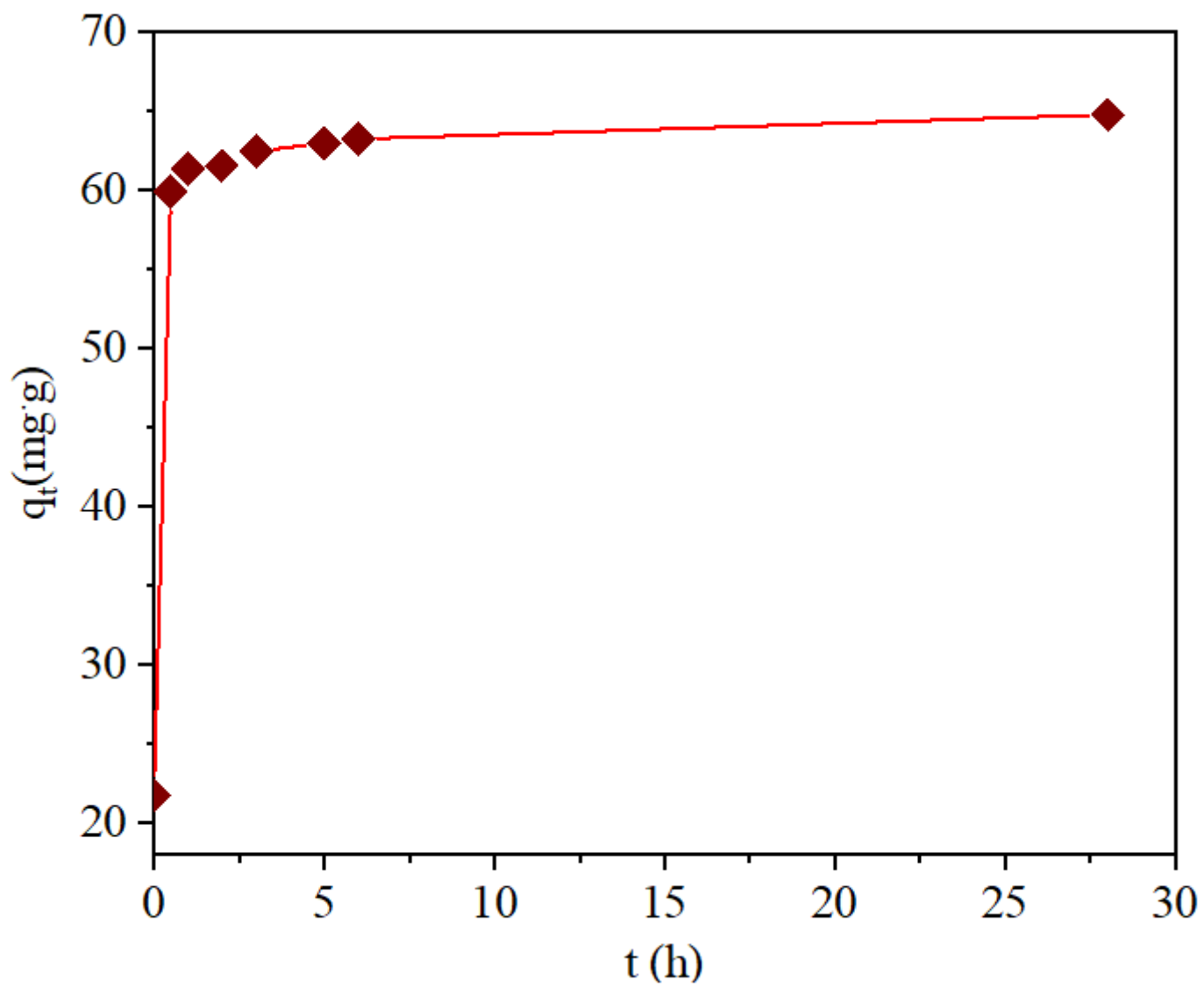


**Figure 8**

The effect of contact time on the adsorption capacity ( $q$ ) of CR (reaction conditions: [dye]=0.1 g.L<sup>-1</sup>, [adsorbent]=0.05 g, T=298 K, pH=3.0).

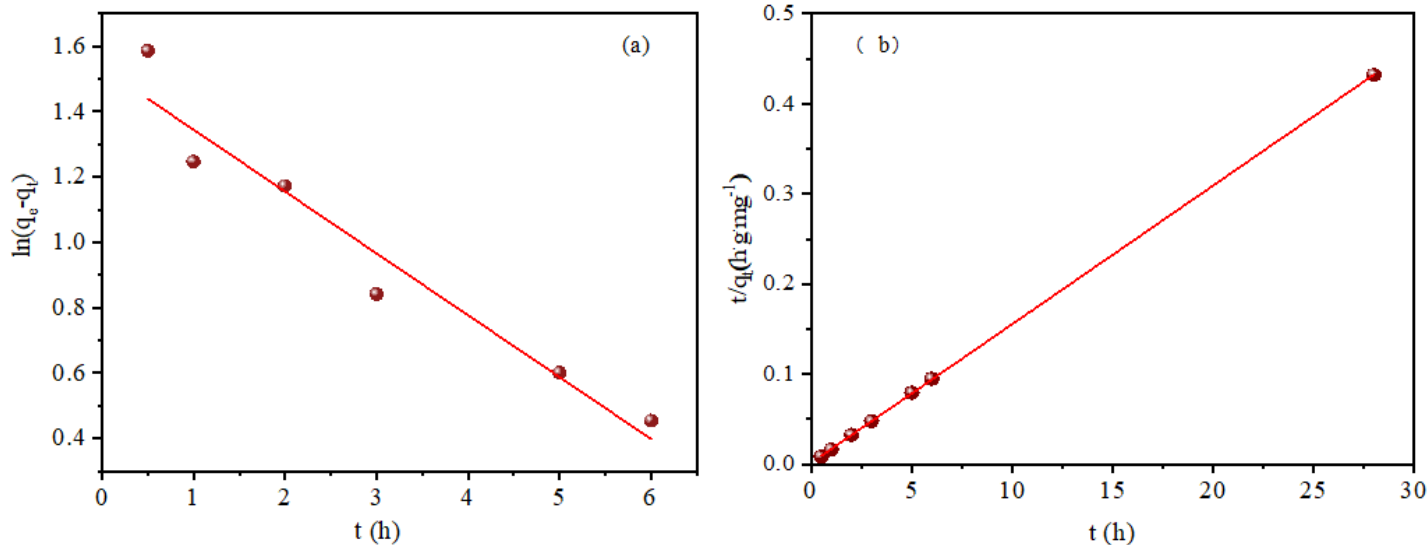


**Figure 9**

Pseudo-first-order (a) and pseudo-second-order (b) kinetics of CR adsorption on MnFe<sub>2</sub>O<sub>4</sub>@Cel-g-p(AA-DMC). (reaction conditions: [dye]=0.1 g.L<sup>-1</sup>, [adsorbent]=0.05 g, T=298 K, pH=3.0).

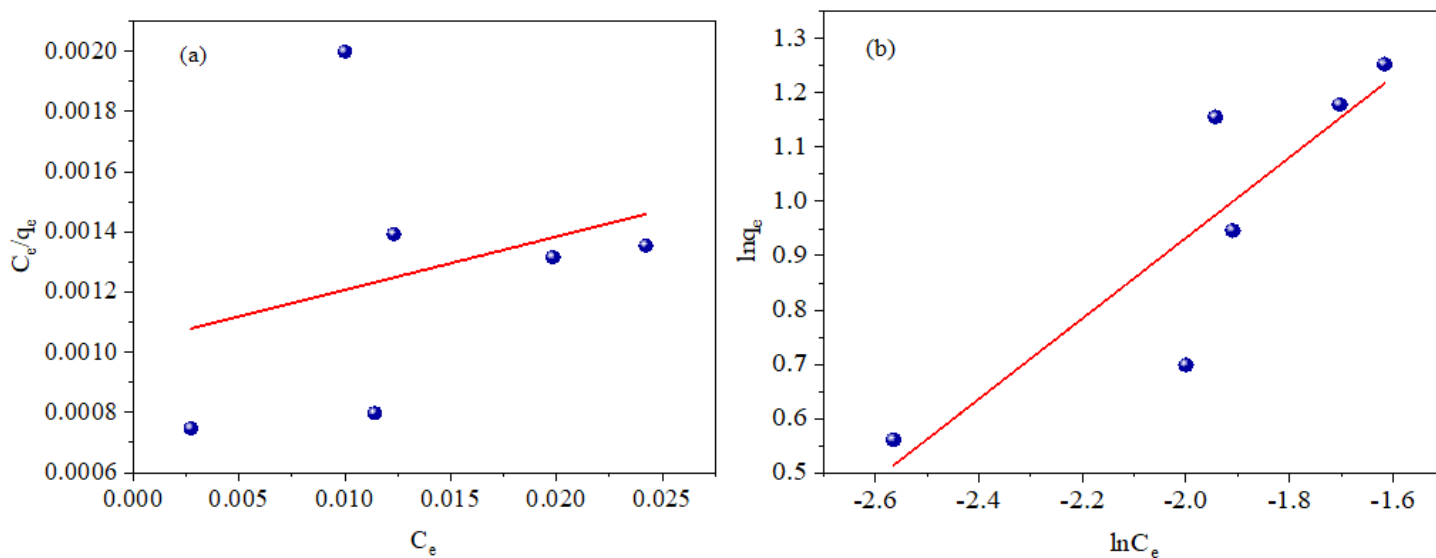


**Figure 10**

Langmuir (a) and Freundlich (b) isotherm curves of CR adsorption on MnFe<sub>2</sub>O<sub>4</sub>@Cel-g-p(AA-DMC). (reaction conditions: [adsorbent]=0.05 g, T=298 K, pH=3.0).

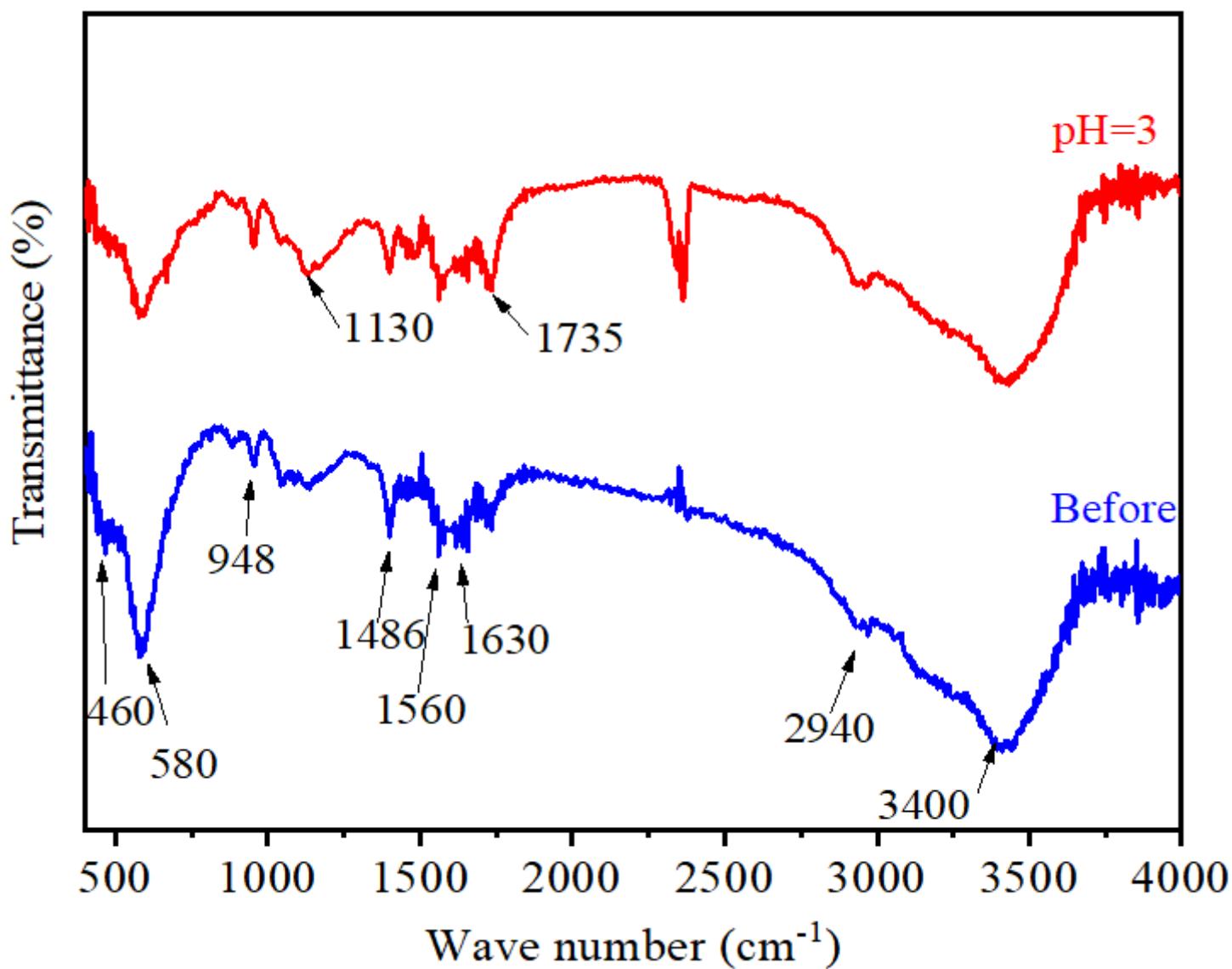


Figure 11

FT-IR spectra of the  $\text{MnFe}_2\text{O}_4@\text{Cel-g-p(AA-DMC)}$  before and after CR adsorption.

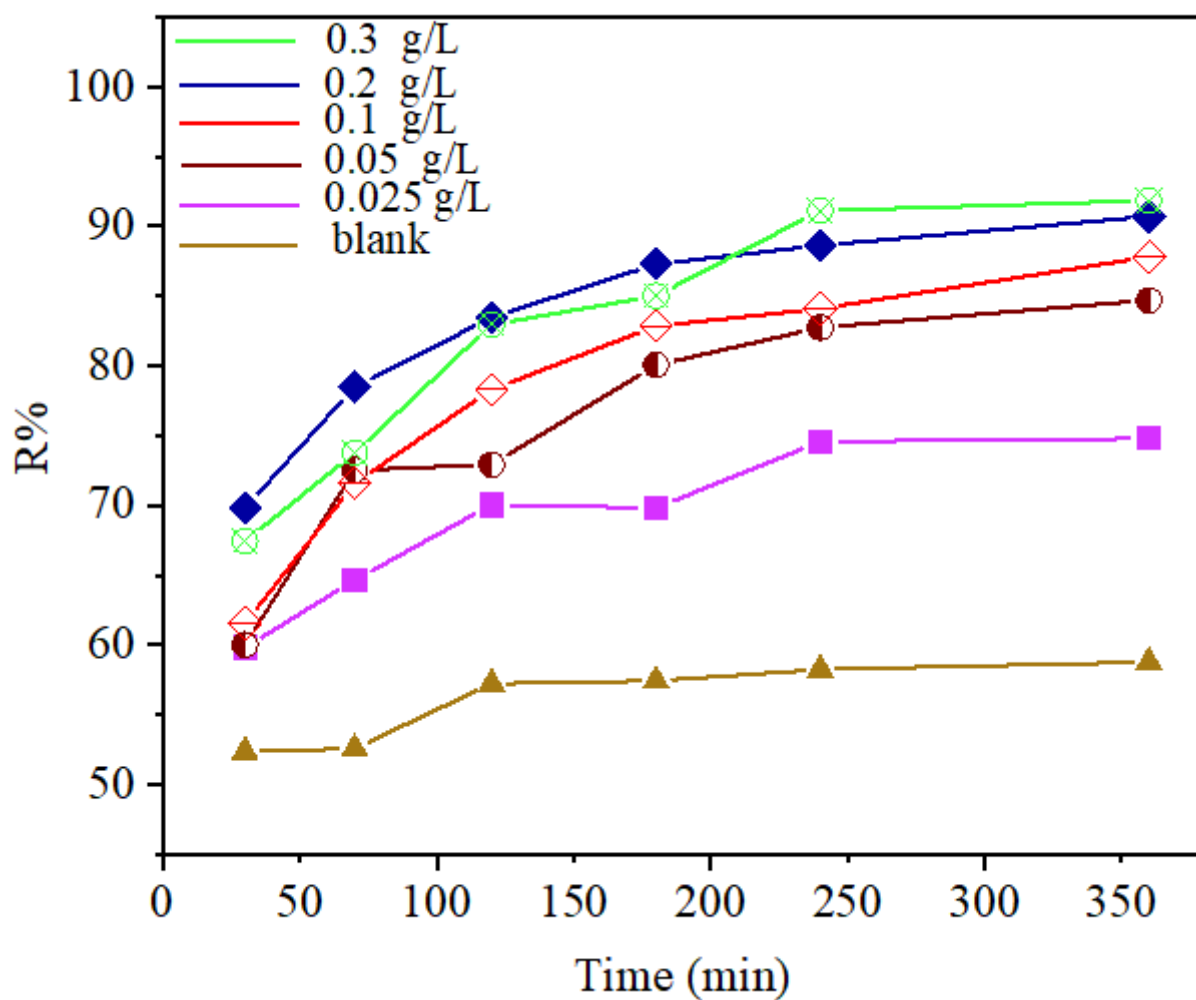


Figure 12

The effect of catalyst dosage on the removal efficiency (R%) of CR (reaction conditions: [dye]=0.08 g.L<sup>-1</sup>, [adsorbent]=0.05 g, T=298 K, pH=3.0).

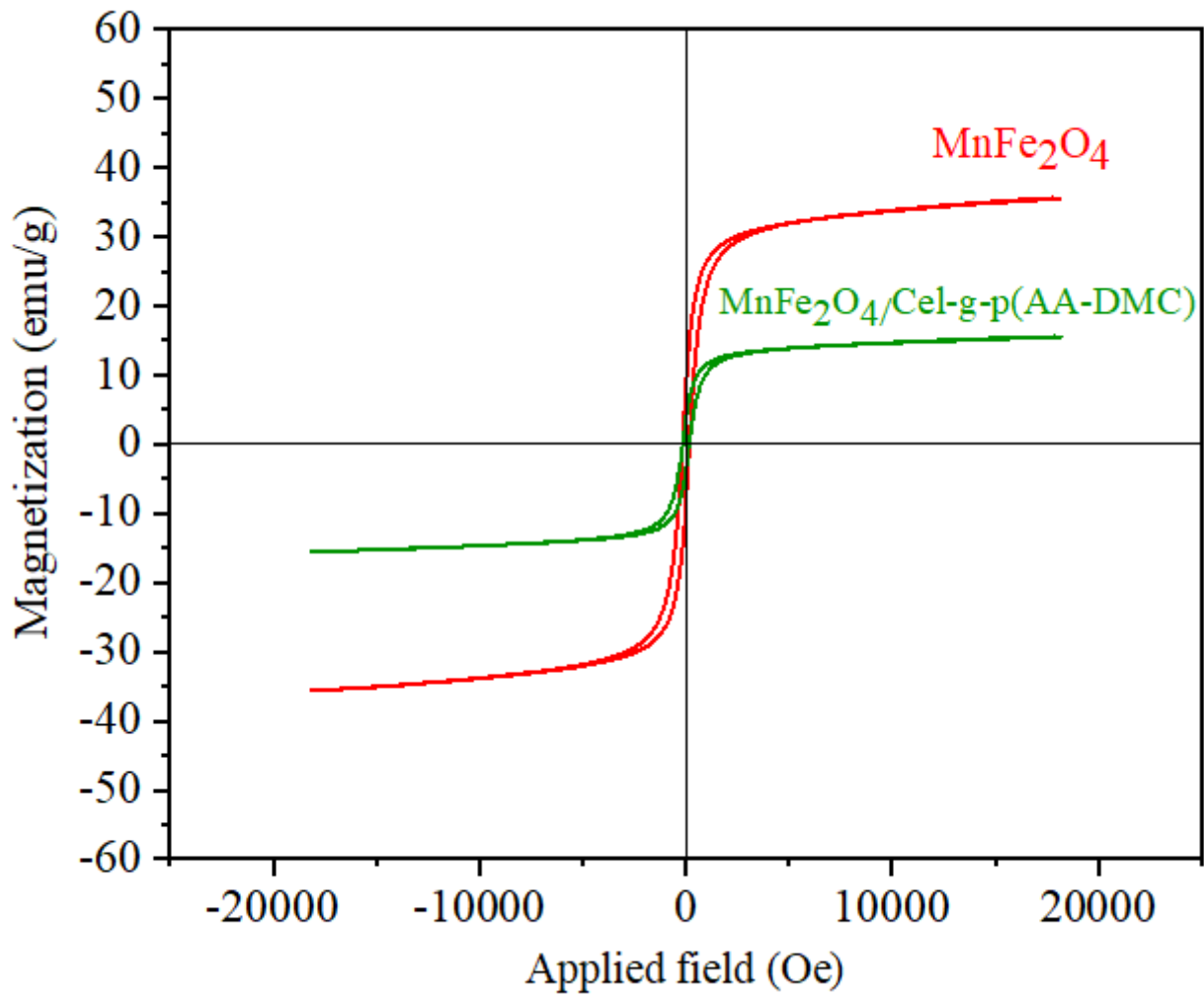
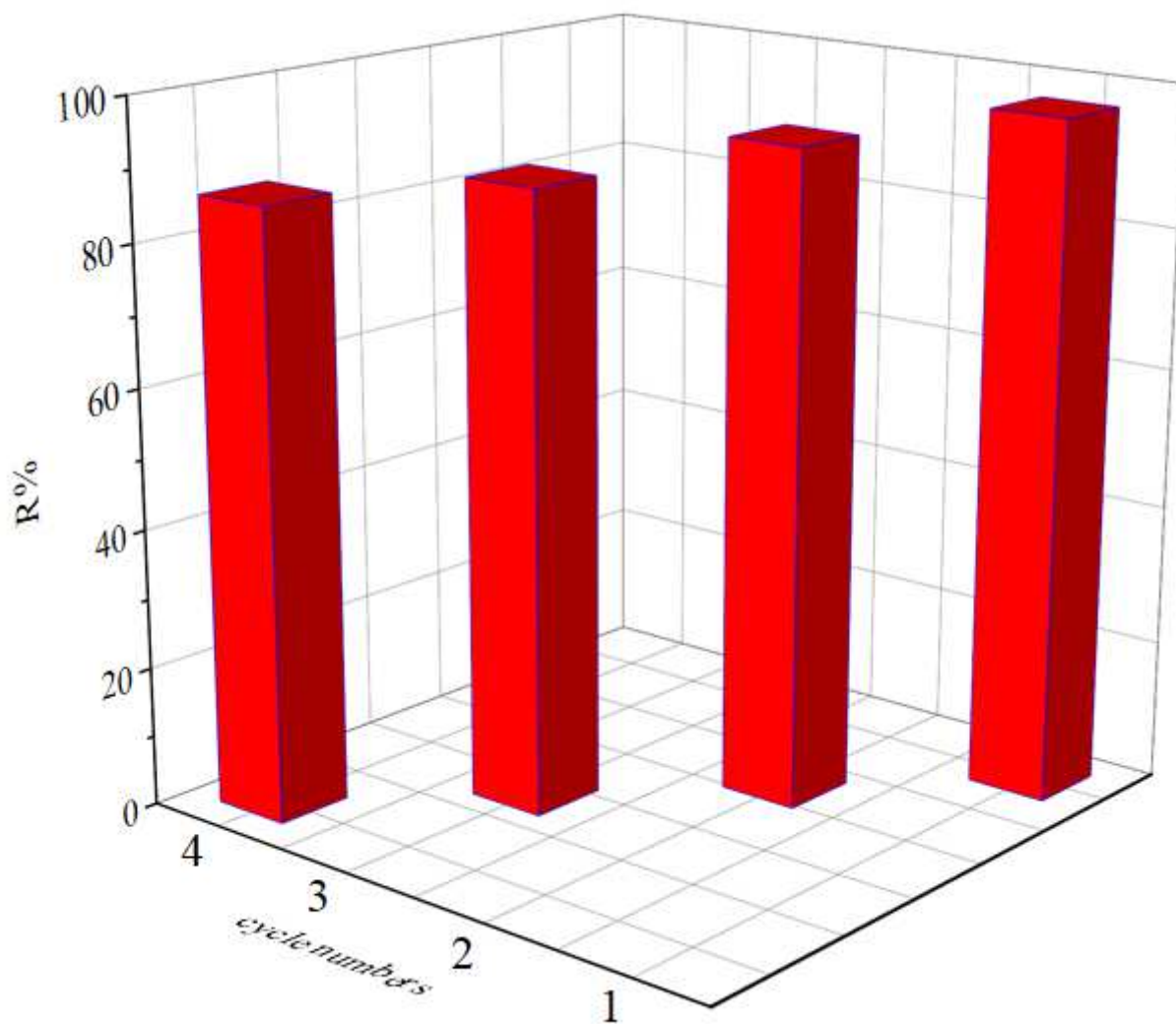


Figure 13

Magnetization property of the MnFe<sub>2</sub>O<sub>4</sub> and MnFe<sub>2</sub>O<sub>4</sub>@Cel-g-p(AA-DMC), inset image of MnFe<sub>2</sub>O<sub>4</sub>@Cel-g-p(AA-DMC) dispersed in wastewater and separated from wastewater under an external magnetic field.



**Figure 14**

Removal efficiency of MnFe<sub>2</sub>O<sub>4</sub>@Cel-g-p(AA-DMC) with multiple cycles of regeneration. (reaction conditions: [dye]=0.08 g.L<sup>-1</sup>, [adsorbent]=0.05 g, T=298 K, pH=3.0).

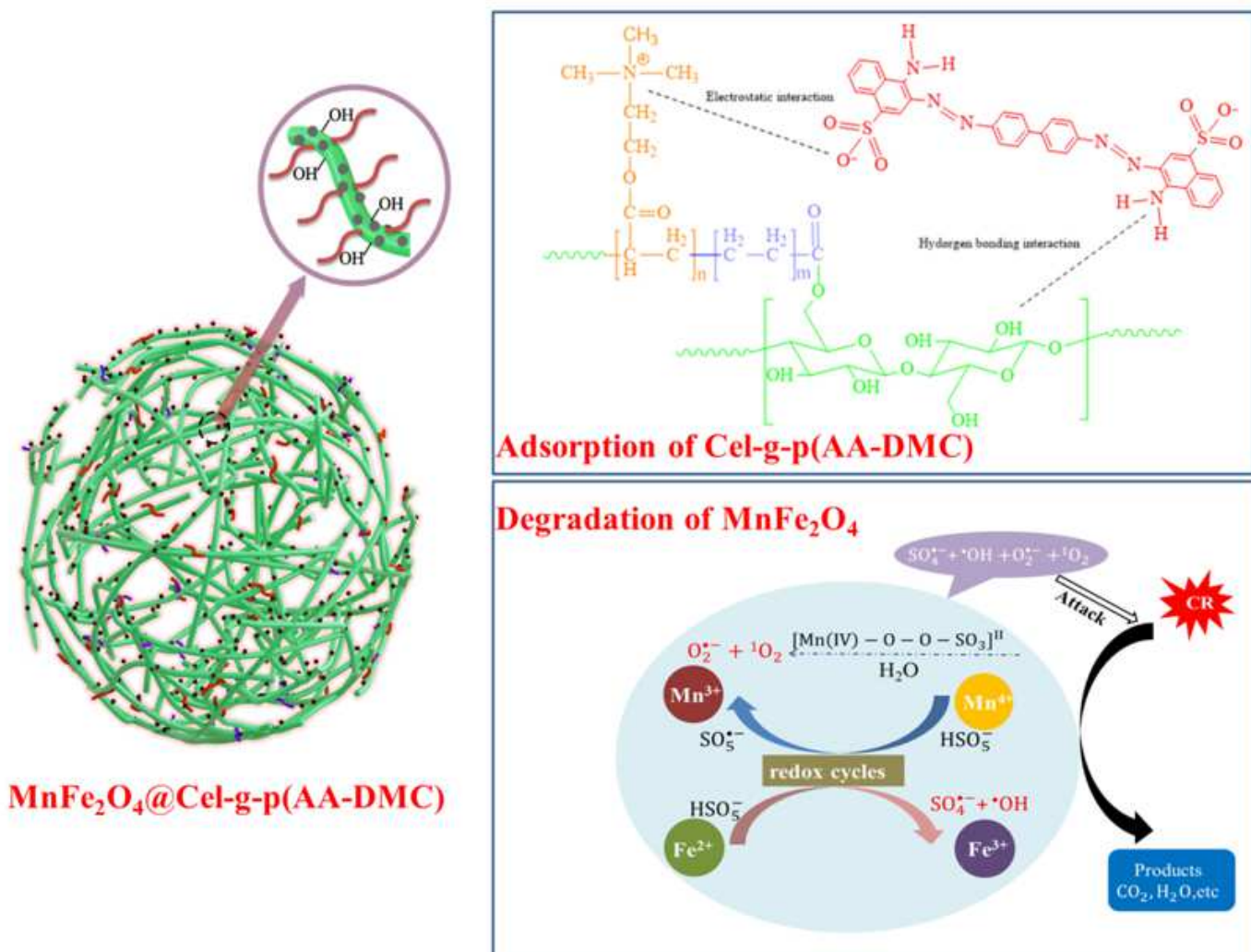


Figure 15

Possible mechanism diagram of MnFe<sub>2</sub>O<sub>4</sub>@Cel-g-p(AA-DMC)/PMS system for the adsorption of Congo red dye.